17

Passive Polarimetric Imaging

Daniel A. LeMaster and Michael T. Eismann
Air Force Research Laboratory, USA

17.1 Introduction

The polarization properties of emitted, reflected, and scattered light are useful tools in remote sensing. These properties are inferred from a collection of radiometric measurements made by a device called a polarimeter. An imaging polarimeter extends this collection of measurements over a two-dimensional array of samples.

Imaging polarimetry has applications extending from medical diagnostics to astronomy. This chapter is devoted to the specific topic of passive broadband electro-optical and infrared Stokes imaging polarimetry for surveillance and reconnaissance in natural environments. Within this scope, there are numerous applications including clutter suppression and contrast enhancement [1–6], image segmentation [7], material characterization [8–10], shape extraction [11], and imaging through scattering media [12, 13]. Additional applications exists and, even among the applications specified, this list is reductive.

Though much of the material presented here is independent of any particular sensor, the scope of this chapter is limited in its discussion of architectures for polarization imagers. Sections 17.5 and 17.6 concentrate on modulated polarimeter technology. For instance, rotating analyzer and microgrid polarimeters are considered from both a data reduction matrix point of view and as linear systems using Fourier analysis. These architectures are most familiar to the authors though perhaps other architectures are better for certain applications.

There are several other very worthwhile resources from eminent authors that the reader is encouraged to explore. Reference [14] is probably the earliest book on the topic of imaging polarimetry and it contains an extensive survey of the work done in the 1980s and prior decades. More recently, [15] is highly recommend as a survey of passive imaging polarimetry up until 2006 and especially for its analysis of imaging polarimeter architectures. A very good treatment of reflective and emissive polarimetric phenomenology and radiative transfer is found in [16]. Excellent and often cited references on polarization science and polarimetry (though not polarization imaging) include [17] and [18]. Our goals in this chapter are to

Multi-dimensional Imaging, First Edition. Edited by Bahram Javidi, Enrique Tajahuerce and Pedro Andrés.

concisely cover all of the important topics required for working in this field, expand on some underrepresented points, and to highlight what is new over the last several years.

17.2 Representations of Polarized Light

The purpose of this section is to discuss the nature of polarization and to solidify the physical concepts of polarized, partially polarized, and unpolarized light. It will quickly become clear that a representation based on electric fields will not be up to the task. The electric field representation will be traded for the Stokes parameters that represent polarized light in terms of measurable radiometric quantities. The interaction of polarized light with matter is then described in terms of Mueller matrices. This Stokes–Mueller formalism will be used throughout the chapter.

17.2.1 Optical Electro-Magnetic Fields

At any fixed point in free space, an optical electro-magnetic field may be described by a pair of orthogonal electric field components of the form,

$$E_x(t) = Re\left[A_x(t)e^{i\delta_x(t)}e^{2\pi i\nu t}\right] \tag{17.1}$$

where $A_x(t)$ is the amplitude of the field at time t, $\delta_x(t)$ is its phase, and ν is the frequency of field oscillation (or the center frequency for polychromatic radiation). Strictly speaking, Eq. 17.1 is valid when the field's spectral bandwidth, $\Delta\nu$, is much smaller than ν [19]. This "narrowband" restriction will be removed later on but, for now, it is useful for illustrating an important point. Once a coordinate system is established, the field components are labeled E_h for the horizontally oriented component and E_v for the vertically oriented component. E_h and E_v are perpendicular to the direction of propagation.

For monochromatic radiation, $A_x(t)$ and $\delta_x(t)$ are constants with time and, when $E_h(t)$ and $E_v(t)$ are plotted parametrically, they form the familiar polarization ellipse [20],

$$\left(\frac{E_h(t)}{A_h}\right)^2 + \left(\frac{E_v(t)}{A_v}\right)^2 - 2\frac{E_h(t)E_v(t)}{A_hA_v}\cos(\delta_v - \delta_h) = \sin^2(\delta_v - \delta_h). \tag{17.2}$$

The time dependence of the amplitude and phase has been intentionally dropped to emphasize that these terms are constant. As shown in Fig. 17.1, this ellipse can also be described by an orientation angle, ψ, and an ellipticity angle, χ,

$$\psi = \frac{1}{2}\arctan\left[\frac{2A_hA_v}{A_h^2 - A_v^2}\cos(\delta_v - \delta_h)\right], \tag{17.3}$$

and

$$\chi = \frac{1}{2}\arcsin\left[\frac{2A_hA_v}{A_h^2 + A_v^2}\sin(\delta_v - \delta_h)\right]. \tag{17.4}$$

ψ is restricted to the range $(0, \pi)$ and the range of χ is $\left(-\frac{\pi}{4}, \frac{\pi}{4}\right)$. ψ defines the direction in which the EM field will exert maximum force and χ describes how the direction of the force evolves with time. The polarization state is said to be "right-handed" when $\chi > 0$ or

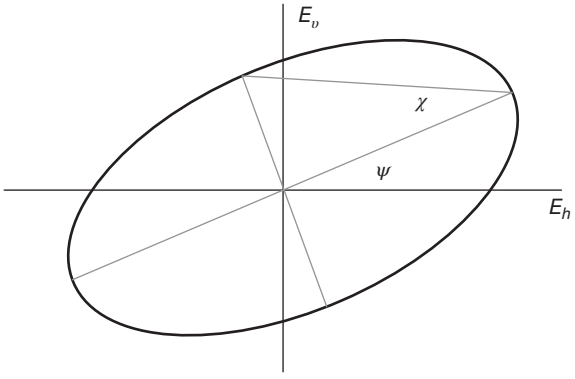

Figure 17.1 Polarization ellipse for monochromatic radiation

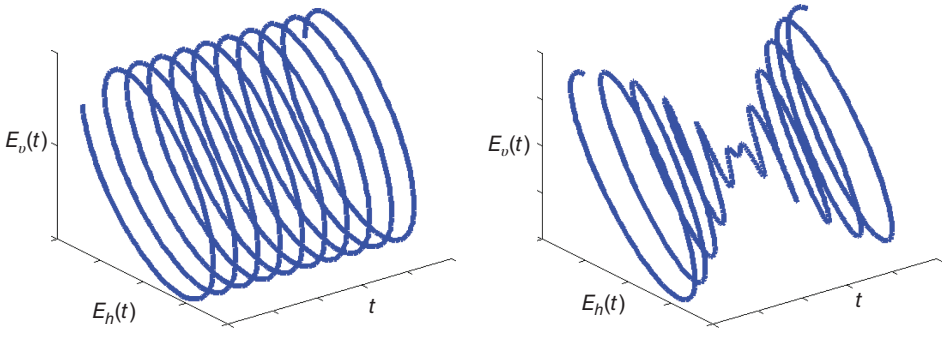

Figure 17.2 Time varying EM fields. Monochromatic radiation (*left*) and a mixture of frequencies with time varying phase (*right*)

"left-handed" when $\chi < 0$. This handedness refers to the direction through which the field orientation rotates as seen by the observer. In cases where $\chi = 0$, the ellipse collapses into linear polarization states.

The EM fields encountered in passive polarimetric imaging are polychromatic and generally have amplitude and phase terms that vary with time. Figure 17.2 shows a monochromatic EM field that may be fully described by the polarization ellipse on the left and a field that is a mixture of two frequencies with a linearly time vary phase on the right. A single polarization ellipse does not characterize this latter type of EM field as it evolves. While ψ and χ can be retained in some sense, this example demonstrates the need to adopt a more robust way to characterize polarization. The next section will provide one method for achieving this goal, the Stokes parameters.

17.2.2 Stokes Parameters and Mueller Matrices

Stokes parameters and Mueller matrices are used widely for polarization problems in remote sensing. The Stokes parameters are useful because they efficiently represent any kind of EM

field described by Eq. 17.1 over realistic measurement intervals and may be inferred from simple linear combinations of directly measurable radiometric quantities. The interactions of Stokes parameters with the physical world are modeled through Mueller matrix transformations. Derivation of the Stokes parameters from electromagnetic principles can be found in [17]. For the present work, the Stokes–Mueller formalism is introduced only to the extent that it will be useful for solving problems later on.

The Stokes parameters fully describe polarization using the second-order statistics of the field. In terms of Eq. 17.1 the Stokes parameters are defined as,

$$S_0 = \langle \tilde{E}_h(t)\tilde{E}_h^*(t)\rangle + \langle \tilde{E}_v(t)\tilde{E}_v^*(t)\rangle \tag{17.5}$$

$$S_1 = \langle \tilde{E}_h(t)\tilde{E}_h^*(t)\rangle - \langle \tilde{E}_v(t)\tilde{E}_v^*(t)\rangle \tag{17.6}$$

$$S_2 = \langle \tilde{E}_h(t)\tilde{E}_v^*(t)\rangle + \langle \tilde{E}_v(t)\tilde{E}_h^*(t)\rangle \tag{17.7}$$

$$S_3 = i\left(\langle \tilde{E}_h(t)\tilde{E}_v^*(t)\rangle - \langle \tilde{E}_v(t)\tilde{E}_h^*(t)\rangle\right) \tag{17.8}$$

where $\langle . \rangle$ is the time average over some measurement interval (an interval that is long compared to the fundamental period of the EM field) and $\tilde{E}_x(t)$ is the complex analytic portion of the optical EM field, that is, $E_x(t) = Re[\tilde{E}_x(t)]$. Note that no assumption has been made regarding spectral bandwidth or about any component of $E_x(t)$ that varies over the measurement interval.

The Stokes parameters may be cast into other useful physical quantities. The first parameter, S_0, is proportional to the magnitude of the Poynting vector. S_0 is always positive and

$$S_0^2 \geq S_1^2 + S_2^2 + S_3^2 \tag{17.9}$$

The remaining parameters are interpreted as:

$$S_1 = PS_0 \cos 2\chi \cos 2\psi \tag{17.10}$$

$$S_2 = PS_0 \cos 2\chi \sin 2\psi \tag{17.11}$$

$$S_3 = PS_0 \sin 2\chi \tag{17.12}$$

where, in additional to time-averaged orientation and ellipticity, a new term, P is defined to be the *Degree of Polarization* (DOP) on the interval $(0, 1)$. In terms of the Stokes parameters,

$$P = \frac{\sqrt{S_1^2 + S_2^2 + S_3^2}}{S_0} \tag{17.13}$$

The term "unpolarized light" is often used to describe the $P = 0$ case but, strictly speaking, $P = 0$ is a case of no preferred polarization over the measurement interval. This case is also sometimes referred to as "randomly polarized". When $P = 1$, the radiation is said to be "fully polarized" and anything in between is said to be "partially polarized". A commonly used and closely related term is the *Degree of Linear Polarization* (DOLP),

$$P = \frac{\sqrt{S_1^2 + S_2^2}}{S_0}. \tag{17.14}$$

Parameters S_1 and S_2 describe the time average orientation direction while S_3 is affiliated with the time averaged ellipticity. When only S_0 and one other parameter are non-zero:

- S_1 by itself describes horizontal ($S_1 > 0$) or vertical ($S_1 < 0$) states
- S_2 by itself describes $+45°$ ($S_2 > 0$) or $-45°$ ($S_2 < 0$) states
- S_3 by itself describes right circular ($S_3 > 0$) or left circular ($S_3 < 0$) states.

The interaction of the Stokes parameters with their environment is modeled using Mueller matrices, $\boldsymbol{M}$, and Stokes vectors, $\mathbf{S}$,

$$\mathbf{S}^{(out)} = \boldsymbol{M}\mathbf{S}^{(in)} = \begin{bmatrix} m_{00} & m_{01} & m_{02} & m_{03} \\ m_{10} & m_{11} & m_{12} & m_{13} \\ m_{20} & m_{21} & m_{22} & m_{23} \\ m_{30} & m_{31} & m_{32} & m_{33} \end{bmatrix} \begin{bmatrix} S_0 \\ S_1 \\ S_2 \\ S_3 \end{bmatrix}, \tag{17.15}$$

where superscripts (*in*) and (*out*) are used to indicate the original and transformed Stokes vectors. The set of all Stokes vectors does not meet the requirement to form a vector space [21] (e.g., since S_0 is always positive, this set contains no inverse elements). Nonetheless the term "Stokes vector" is in consistent widespread use.

For incoherent radiation, Stokes parameters from two (or more) sources combine via vector addition (i.e., element-wise addition). The Stokes–Mueller formalism may also be used to solve some problems dealing in coherent radiation but, to sum coherent radiation, the Jones calculus [17] must be used instead.

Each element in an optical system has a corresponding Mueller matrix. The cumulative effects of these individual Mueller matrices are found through matrix multiplication. For example, if Stokes vector $\mathbf{S}^{(in)}$ interacts with optical element 1 before element 2 then

$$\mathbf{S}^{(out)} = \boldsymbol{M}_2\boldsymbol{M}_1\mathbf{S}^{(in)}. \tag{17.16}$$

This matrix product does not commute.

The example Mueller matrices in Eqs. 17.17–17.19 will be useful for describing the polarimeters in Section 17.5. $\boldsymbol{M}_D$ is the Mueller matrix of a linear diattenuator,

$$\boldsymbol{M}_D(p_h, p_v) = \frac{1}{2}\begin{bmatrix} p_h^2 + p_v^2 & p_h^2 - p_v^2 & 0 & 0 \\ p_h^2 - p_v^2 & p_h^2 + p_v^2 & 0 & 0 \\ 0 & 0 & 2p_h p_v & 0 \\ 0 & 0 & 0 & 2p_h p_v \end{bmatrix} \tag{17.17}$$

where p_h and p_v are electric field amplitude attenuation coefficients for polarization in the horizontal and vertical directions. A linear diattenuator is often referred to as a polarizer.

Next is the retarder,

$$\boldsymbol{M}_W(\delta) = \begin{bmatrix} 1 & 0 & 0 & 0 \\ 0 & 1 & 0 & 0 \\ 0 & 0 & \cos\delta & \sin\delta \\ 0 & 0 & -\sin\delta & \cos\delta \end{bmatrix} \tag{17.18}$$

where δ is additional phase delay imposed on the h component of the optical electric field relative to the v component. An example of a device with a fixed retardance at a given wavelength is a wave plate. Other devices, such as liquid crystals, may be operated in a variable retardance mode.

Matrix $\boldsymbol{M}_R$ rotates a Stokes vector through angle θ about the optical axis.

$$\boldsymbol{M}_R(\theta) = \begin{bmatrix} 1 & 0 & 0 & 0 \\ 0 & \cos 2\theta & \sin 2\theta & 0 \\ 0 & -\sin 2\theta & \cos 2\theta & 0 \\ 0 & 0 & 0 & 1 \end{bmatrix} \tag{17.19}$$

This Mueller matrix is particularly useful for interactions with elements that are more simply described in rotated coordinate system. For instance, the Mueller matrix of a linear diattenuator that is rotated by θ from the horizontal is given by

$$\boldsymbol{M}_R(-\theta)\boldsymbol{M}_D(p_h, p_v)\boldsymbol{M}_R(\theta) \tag{17.20}$$

17.2.3 The Poincaré Sphere

The Poincaré sphere is a useful tool for visualizing how polarization states change as system parameters vary. As shown in Fig. 17.3, the Poincaré coordinate system is composed of the Stokes parameters S_1, S_2, and S_3. Stokes vectors plotted on the sphere are normalized so that $S_0 = 1$ and only fully polarized light ($P = 1$) is represented on this surface. The longitude of a point on the sphere is twice the orientation angle as measured from the positive S_1 axis. Similarly, latitude is given by twice the ellipticity angle as measured from the S_1,S_2 plane. An application of the Poincaré sphere is found later in Section 17.5.2.

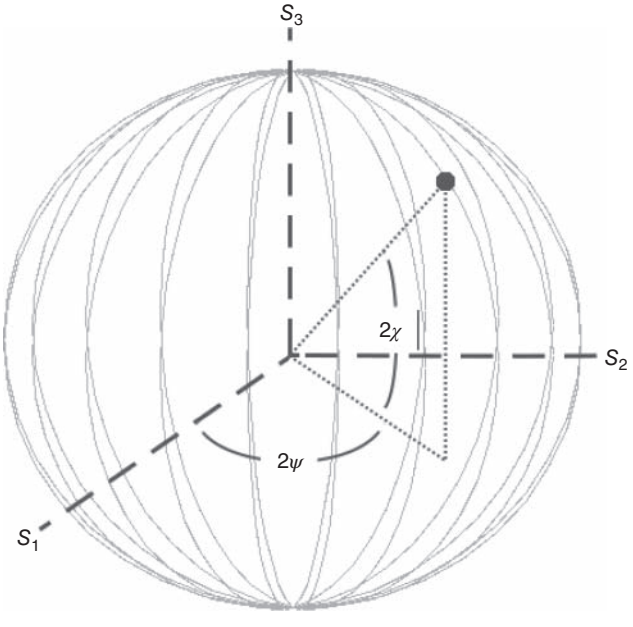

Figure 17.3 A fully polarized Stokes vector is a point on the Poincaré sphere

17.3 Polarized Reflection and Emission

Different materials and surfaces reflect and emit light in different ways. These differences are responsible for the polarization contrast exploited in imaging polarimetry. The purpose of this section is to introduce these concepts using the Stokes–Mueller calculus and to draw some specific conclusions on how to exploit these phenomena.

17.3.1 Reflection

At wavelengths shorter than 3 μm, an object's polarization signature is dominated by reflection and scattering at or near its surface. Surface reflections are often modeled by Fresnel's laws applied in a statistical sense to the various microscopic facets of the target surface. Light that penetrates the surface is either absorbed or scattered in the bulk of the material. Some of this bulk scattered light is transmitted back out in what is often a depolarizing process. The combined effects of surface and bulk reflections are modeled by the *Bidirectional Reflectance Distribution Function* (BRDF) Mueller matrix. The element in the x^{th} row and y^{th} column in this Mueller matrix is defined to be:

$$f_{xy}(\theta_i, \phi_i, \theta_r, \phi_r, \lambda) = \frac{\mathrm{d}L_x(\theta_r, \phi_r, \lambda)}{\mathrm{d}E_y(\theta_i, \phi_i, \lambda)} \tag{17.21}$$

where L_x is the radiance in Stokes parameter x reflected into direction (θ_r, ϕ_r) given an input irradiance, E_y, in Stokes parameter y incident from direction (θ_i, ϕ_i) at wavelength λ. By convention, angles θ_i and θ_r are the elevation angles of the incident and reflected light measured from the target surface normal direction. Angles ϕ_i and ϕ_r are the azimuth angles of the incident and reflected light. The BRDF elements have units of inverse steradians. The target reflected Stokes vector, $\mathbf{S}^{(r)}$, is calculated from the BRDF and the incident Stokes vectors, $\mathbf{S}^{(i)}$, arriving from around the hemisphere

$$\mathbf{S}^{(r)}(\theta_r, \phi_r, \lambda) = \int_0^{2\pi} \int_0^{\frac{\pi}{2}} \boldsymbol{f}(\theta_i, \phi_i, \theta_r, \phi_r, \lambda)\mathbf{S}^{(i)}(\theta_i, \phi_i, \lambda) \cos\theta_i \sin\theta_i \mathrm{d}\theta_i \mathrm{d}\phi_i. \tag{17.22}$$

In this equation, all Stokes vector components are in units of radiance.

Polarimetric BRDFs have been proposed for a variety of applications. Here, we will consider a simplified empirical BRDF model based on the microfacet model [22] with an added term for diffuse depolarization to demonstrate a few salient points,

$$\boldsymbol{f} = \boldsymbol{d} + \boldsymbol{M}_{fr}(\beta, \hat{n}) \frac{o(\alpha, b, \sigma)}{4\cos(\theta_i)\cos(\theta_r)} \tag{17.23}$$

where $\boldsymbol{d}$ is a depolarizing Mueller matrix that lumps together all bulk and diffuse surface reflections. In $\boldsymbol{d}$, the only nonzero element is $m_{00} = d$. $\boldsymbol{M}_{fr}$ is the Mueller matrix for Fresnel reflection and o is the microfacet orientation distribution function. Explicit dependence on the incident and reflected angles has been suppressed for clarity. Each of these terms, their meanings, and their associated parameters are described next.

The Fresnel reflection Mueller matrix is

$$\boldsymbol{M}_{fr}(\beta,\hat{n}) = \frac{1}{2}\begin{bmatrix} r_s r_s^* + r_p r_p^* & r_s r_s^* - r_p r_p^* & 0 & 0 \\ r_s r_s^* - r_p r_p^* & r_s r_s^* + r_p r_p^* & 0 & 0 \\ 0 & 0 & 2\mathrm{Re}(r_s r_p *) & 2\mathrm{Im}(r_s r_p *) \\ 0 & 0 & -2\mathrm{Im}(r_s r_p *) & 2\mathrm{Re}(r_s r_p *) \end{bmatrix} \tag{17.24}$$

with Fresnel amplitude reflection coefficients [23]

$$r_s = \frac{\cos\beta - \sqrt{\hat{n}^2 - \sin^2\beta}}{\cos\beta + \sqrt{\hat{n}^2 - \sin^2\beta}} \tag{17.25}$$

$$r_p = \frac{\hat{n}^2\cos\beta - \sqrt{\hat{n}^2 - \sin^2\beta}}{\hat{n}^2\cos\beta + \sqrt{\hat{n}^2 - \sin^2\beta}} \tag{17.26}$$

where $\hat{n}$ as the relative refractive index, $\hat{n} = \frac{n_2}{n_1}$. Index n_2 is the reflecting media and n_1 is the index of the surrounding atmosphere. These refractive indices are, in general, complex. The subscript s refers to the amplitude reflection coefficient for the electric field component perpendicular to the plane of incidence (the plane containing the incident and reflected beams). In other words, the s direction is parallel to the surface. Subscript p is the reflection coefficient for the electric field component that is perpendicular to the s direction. It is important to note that the Fresnel Mueller matrix and, by extension, the BRDF is defined with respect to the orientation of the reflecting surface.

Several useful points need to be made about the physics of Fresnel reflections. First,

$$r_s r_s^* \geq r_p r_p^*, \tag{17.27}$$

so randomly polarized light (e.g., from the Sun) tends to become s-polarized upon reflection. In the reference frame of the surface, this is also the positive S_1 direction. Second, Fresnel reflections from non-absorbing materials (real refractive index) tend to be less reflective but more strongly polarizing. Conversely, strongly absorbing materials (large imaginary refractive index component) are strongly reflective but less polarizing. Finally, the extent to which reflected light is polarized is heavily dependent on the incidence angle β. All of these points are demonstrated in Fig. 17.4 for silicon dioxide ($\hat{n} = 1.46$) and gold ($\hat{n} = 0.36 + 2.77i$) at 500 nm wavelength.

The Fresnel reflection Mueller matrix also shows that, for isotropic materials, a single reflection will never convert randomly polarized radiation into S_3. This "first surface" reflection dominates many polarization signatures found in nature. As a result, it is often not worth the cost or added complexity required to build an imaging polarimeter that is sensitive to elliptical polarization states.

The microfacet orientation distribution function, o, describes the fractional amount of light that is reflected into direction (θ_r, ϕ_r) from direction (θ_i, ϕ_i) due to facets oriented with an angular surface normal deviation of α from the average local surface normal. The relationships between all of the angles involved in the definition of the BRDF are

$$\cos\alpha = \frac{\cos\theta_i + \cos\theta_r}{2\cos\beta} \tag{17.28}$$

$$\cos(2\beta) = \cos\theta_i\cos\theta_r + \sin\theta_i\sin\theta_r\cos(\phi_i - \phi_r). \tag{17.29}$$

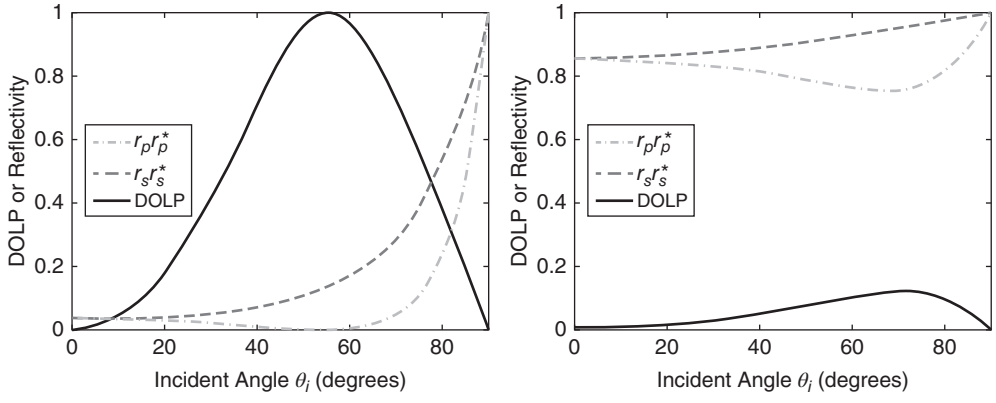

Figure 17.4 Fresnel reflection and DOLP: (*left*) silicon dioxide, (*right*) gold

The microfacet distribution function is assumed to be Gaussian in this model and parameterized by the standard deviation, σ, of the local surface slope, $\tan\alpha$, and a weight, b, which determines the relative strength of the Fresnel component over the diffuse component, $\boldsymbol{d}$.

$$o(\alpha, b, \sigma) = \frac{b}{2\pi\sigma^2 \cos^3\alpha} \exp\left(\frac{-\tan^2\alpha}{2\sigma^2}\right) \tag{17.30}$$

The combined effects of the BRDF model parameters are shown in Fig. 17.5 for surfaces illuminated with randomly polarized light in the forward scattering plane ($|\phi_r - \phi_i| = 180°$). On the left is a near specular surface reflection ($\sigma = 0.05$, $d = 10^{-5}$, and $b = 0.2$) off of silicon dioxide from 30° incidence. The largest reflection occurs in the target average specular direction (shown as −30°). The degree of linear polarization (DOLP) in this direction is about 0.4, which is consistent with a 30° incident angle in Fig. 17.4. DOLP continues to increase as microfacet reflection angle increases but the maximum achievable DOLP is tempered by the grazing angle dominance of the depolarizing diffuse reflection component.

A roughened silicon dioxide surface ($\sigma = 0.1$, $d = 0.03$, and $b = 0.2$) is shown on the right of Fig. 17.5. In this case, there is significant scattering in all directions but polarized reflections are relegated to near the target average specular direction and further muted by the influence of the large diffuse reflection component.

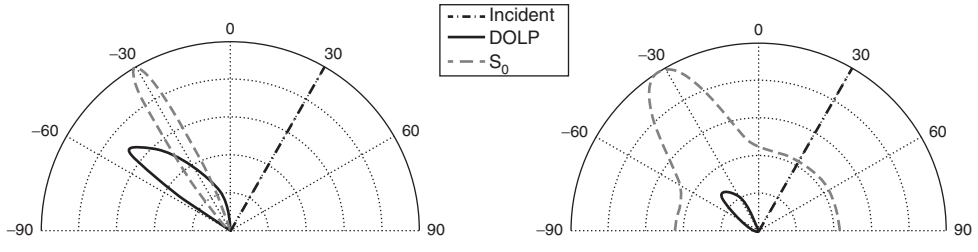

Figure 17.5 Two example cross sections of total radiance (normalized) and degree of linear polarization: (*left*) a near specular surface, (*right*) a roughened surface. In both cases, S_0 peak normalized

This example demonstrates why it is generally inadvisable to collect polarimetric imagery in an orientation with the Sun (or other major illumination source) behind the camera. All of the polarization response is confined to the forward scattering direction. This example also demonstrates why collection of polarization from an airborne platform is best done at a slant angle (where the polarization response will be highest) rather than from nadir (where the image resolution will be highest). This is an important trade off to consider in collection planning. Note that this example does not address reflection contributions from multiple or distributed sources (e.g., skylight), which is a key part of the utility of Eq. 17.22.

Note that the reflected light will be polarized parallel to the microfacet surface defined by the incident and reflected angles. The plane of incidence (which contains the incident, microfacet normal, and reflected directions) is rotated by an angle η with respect to the plane defined by the average target surface normal and the direction of reflection. For an observer using the average target surface normal coordinate system for both the incident and reflected Stokes vectors, the apparent BRDF is

$$\boldsymbol{f}^{global}(\theta_i, \phi_i, \theta_r, \phi_r, \lambda) = \boldsymbol{M}_R(\eta)\boldsymbol{f}(\theta_i, \phi_i, \theta_r, \phi_r, \lambda)\boldsymbol{M}_R(-\eta) \tag{17.31}$$

where M_R is the rotation Mueller matrix from Eq. 17.19. In this coordinate system, a material that obeys a Fresnel microfacet model will shift some reflected light between S_1 and S_2 when illuminated by an unpolarized source and $|\eta| > 0$. There is no geometry where incident unpolarized light will be reflected into S_3. Because α increases as $|\eta|$ increases, the microfacet distribution function will weight the increasing $|\eta|$ contributions to total radiance less heavily.

Figure 17.6 shows a NIR band Stokes images of an object (a black backpack) camouflaged in S_0 by its proximity to the shadows of the trees. It has a low overall reflectivity, which explains why it blends with the shadows, but the sunlight that it reflects is quite clearly polarized. The natural surroundings exhibit only weakly polarized reflections in S_1 and so the target stands out. From the shadow angle, it is clear that the camera is not in the principal plane of the target ($|\eta| > 0$) and so there is a significant S_2 component to the target signature as well.

In this example, a contrast stretch is applied to each Stokes image individually. To provide a better impression of how much polarization content there is in this scene, a DOLP image is provided in Fig. 17.7. This DOLP image is scaled between 0 (randomly polarized) and the peak polarization value of the backpack, about 11%. As a reference point, the next most polarized feature in the scene is the sun-illuminated grass with a DOLP of about 1% or less.

Figure 17.6 NIR polarimetric imagery of a hidden object. S_0 (*left*), S_1 (*middle*), S_2 (*right*)

Figure 17.7 NIR DOLP image of the hidden object in Fig. 17.6

17.3.2 Emission

Objects at terrestrial temperatures spontaneously emit measurable radiation at wavelengths of 3 μm and longer. The amount of radiation emitted at a given wavelength depends on the object's temperature, T, and a object dependent property called emissivity. Like BRDF, emissivity is determined by material type, surface conditions, and viewing orientation. The Stokes vector for emission from a surface is

$$\mathbf{S}^{(e)}(\lambda, T, \theta, \phi) = L_{BB}(T, \lambda)\epsilon(\theta, \phi, \lambda) \tag{17.32}$$

where L_{BB} is the Planck blackbody radiation equation and ϵ is the emissivity vector.

For opaque materials, randomly polarized emission occurring within approximately one skin depth of the surface will become partially polarized upon transmission across the surface boundary [24]. Because of this, the emissivity vector ϵ is the first column of the Mueller matrix representing this boundary transmission.

$$\epsilon(\theta, \phi, \lambda) = \boldsymbol{M}_e(\theta, \phi, \lambda)\begin{bmatrix}1\\0\\0\\0\end{bmatrix} \tag{17.33}$$

where $\boldsymbol{M}_e$ is the Mueller matrix for emission.

Two additional facts allow the emissivity vector to be conveniently described in terms of the polarimetric BRDF [25]. All materials exchange perfect blackbody radiation with their surroundings when the entire system is in a state of thermal equilibrium. Furthermore, perfect blackbody radiation is randomly polarized. Therefore, in a chamber at thermal equilibrium,

the following must be true at any temperature:

$$\begin{bmatrix}1\\0\\0\\0\end{bmatrix} = \epsilon(\theta,\phi,\lambda) + \rho(\theta,\phi,\lambda)\begin{bmatrix}1\\0\\0\\0\end{bmatrix} \tag{17.34}$$

where $\rho(\theta,\phi,\lambda)$ is the *Hemispherical Directional Reflectivity* (HDR) Mueller matrix with entries

$$\rho_{xy}(\theta,\phi,\lambda) = \int_0^{2\pi}\int_0^{\frac{\pi}{2}} f_{xy}(\theta_i,\phi_i,\theta,\phi,\lambda)\cos\theta_i \sin\theta_i \mathrm{d}\theta_i \mathrm{d}\phi_i. \tag{17.35}$$

This expression of HDR describes the fraction of total light reflected in direction (θ,ϕ) when the target is illuminated uniformly from all directions. The meaning of Eq. 17.34 is clear–the Stokes vector at any point inside the cavity is randomly polarized (left-hand side); therefore, the sum of all emitted and reflected light must also be randomly polarized for every surface (right-hand side). This is Kirchoff's law, generalized for polarization.

Regardless of the exact polarization BRDF model used,

$$\rho_{30}(\theta,\phi,\lambda) = 0 \tag{17.36}$$

because $f_{30} = 0$ whenever Fresnel reflection is the primary mechanism for polarization (very few naturally occurring exceptions come to mind). Additionally,

$$\rho_{20}(\theta,\phi,\lambda) = 0 \tag{17.37}$$

because of the rotational symmetry of the microfacet distribution. This outcome is consistently observed in nature as well. A complete definition of the emissivity vector now emerges:

$$\epsilon(\theta,\phi,\lambda) = \begin{bmatrix}1-\rho_{00}(\theta,\phi,\lambda)\\-\rho_{10}(\theta,\phi,\lambda)\\0\\0\end{bmatrix}. \tag{17.38}$$

Thus emitted radiation is polarized in the direction of the average target surface normal (i.e., p-polarized). This is the $-S_1$ direction in the coordinate system defined previously for target surfaces. Equation 17.38 is useful in polarimetric remote sensing because it is also a very good approximation of natural emission behavior outside of the theoretical chamber at thermal equilibrium.

Figure 17.8 is an example of emission polarization using the BRDF model in Eq. 17.23 to calculate HDR with parameters $\hat{n} = 1.8 + 1.0i$, $d = 10^{-5}$, $\sigma = 0.05$, and $b = 1$ (i.e., a relatively smooth absorbing material). The dashed curve shows the total emitted radiation normalized by $L_{bb}(T,\lambda)$. Total emission has a broad peak in the surface normal direction (0°) and then falls off gradually with increasing angle. Polarized emission, represented by degree of linear polarization, is zero in the surface normal direction and then increases as the viewing angle increases. This pattern is rotationally symmetric with azimuth and is typical of many processed surfaces and materials. Just like in the reflection case, polarized emission is best viewed at a slanted angle.

All objects simultaneously emit and reflect radiation. To gain an appreciation for the magnitude of these combined effects on polarization signature, consider Fig. 17.9. Here, the material

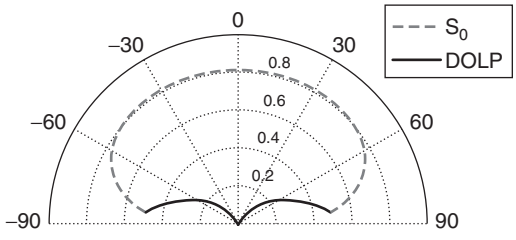

Figure 17.8 An example cross section of total radiance (normalized) and degree of linear polarization for polarized emission

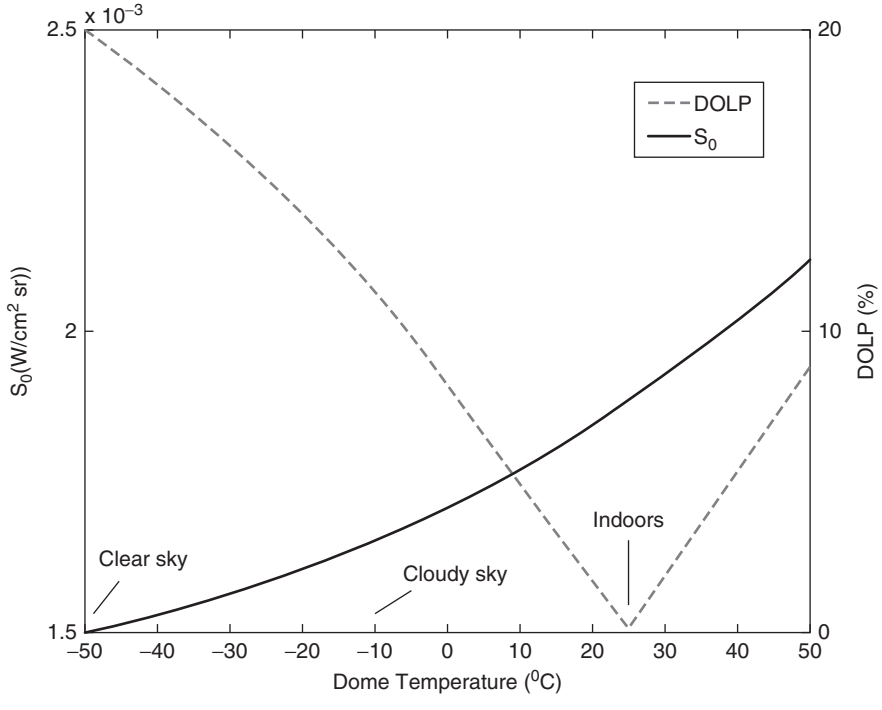

Figure 17.9 Total radiance and DOLP as a function of apparent background temperature. The target temperature is 25°C and observation angle is 60° away from the target surface normal

used in Fig. 17.8 is observed in the LWIR (8 to 10 μm) under a uniform blackbody hemisphere at a look angle of 60°. As the hemisphere warms up, the total apparent target radiance (reflected and emitted) increases and the apparent degree of polarization decreases. The degree of polarization trend reverses once the hemisphere becomes warmer than the target. Past the equilibrium temperature, reflection dominates and the apparent target polarization switches from p-polarized to s-polarized. Atmospheric effects will be dealt with in the following section but some useful apparent temperatures are labeled on the plot for reference. Among other

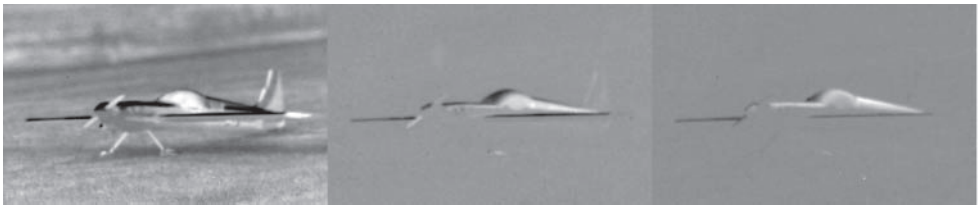

Figure 17.10 LWIR polarimetric imagery of a remote control aircraft. S_0 (*left*), S_1 (*middle*), S_2 (*right*)

things, this plot demonstrates why indoor emissive band polarization imaging is typically muted. Additional discussion on this topic is found in [26].

Any example of a LWIR polarimetric image is shown in Fig. 17.10. The S_1 and S_2 images are scaled so that the darkest regions have the most negative values and the lightest regions are the most positive values. S_0 values are always positive. On the top half of the aircraft, the horizontal surfaces show a preference for the negative S_1 direction and the vertical surfaces show a preference for the positive S_1 direction. Emission on the canopy smoothly transitions from positive to negative S_1 following the curvature. These three observations are consistent with emission from these surfaces being p-polarized (i.e., perpendicular to the surface). On the undercarriage, none of the surfaces show strong polarization because the emitted radiation is mixed with s-polarized reflections of the warm ground. The net result is effectively zero polarization. Note that the ground beyond the aircraft is largely randomly polarized. This is true of many natural backgrounds.

There is polarization content in both S_1 and S_2 because the aircraft surfaces are rotated somewhat with respect to the horizontal and vertical axes of the camera reference frame. It is important to remember that the s and p directions are defined with respect to the surface, not with respect to the camera.

17.4 Atmospheric Contributions to Polarimetric Signatures

The reflection and emission signatures of materials will be altered by the atmosphere. In many cases, these changes are substantial and highly variable. This variability is both temporal, in the sense that atmospheric conditions constantly change, and spatial because each part of the sky affects the target signature in a different way depending on the target BRDF. The radiative transfer equations that describe the polarization effects of the atmosphere are provided in exquisite detail in [16]. In practice, implementing these equations requires extensive measurements and modeling. Many of the required parameters cannot be measured directly without access to the target site.

The following discussion will be divided into polarimetric effects in the reflective bands ($\lambda < 3$ μm) and the emissive bands ($\lambda > 3$ μm). This is a distinction that arises because the remotely sensed radiation at these shorter wavelengths is dominated by solar illumination and scattering, while thermal emission from objects becomes a major component at wavelengths above 3 μm. These spectral regions are further sub-divided by the atmospheric windows; that is, the spectral bands for which the atmosphere has sufficiently small absorption that light reflected or emitted from an object can adequately transmit through it. Figure 17.11 (Plate 29) illustrates the ground

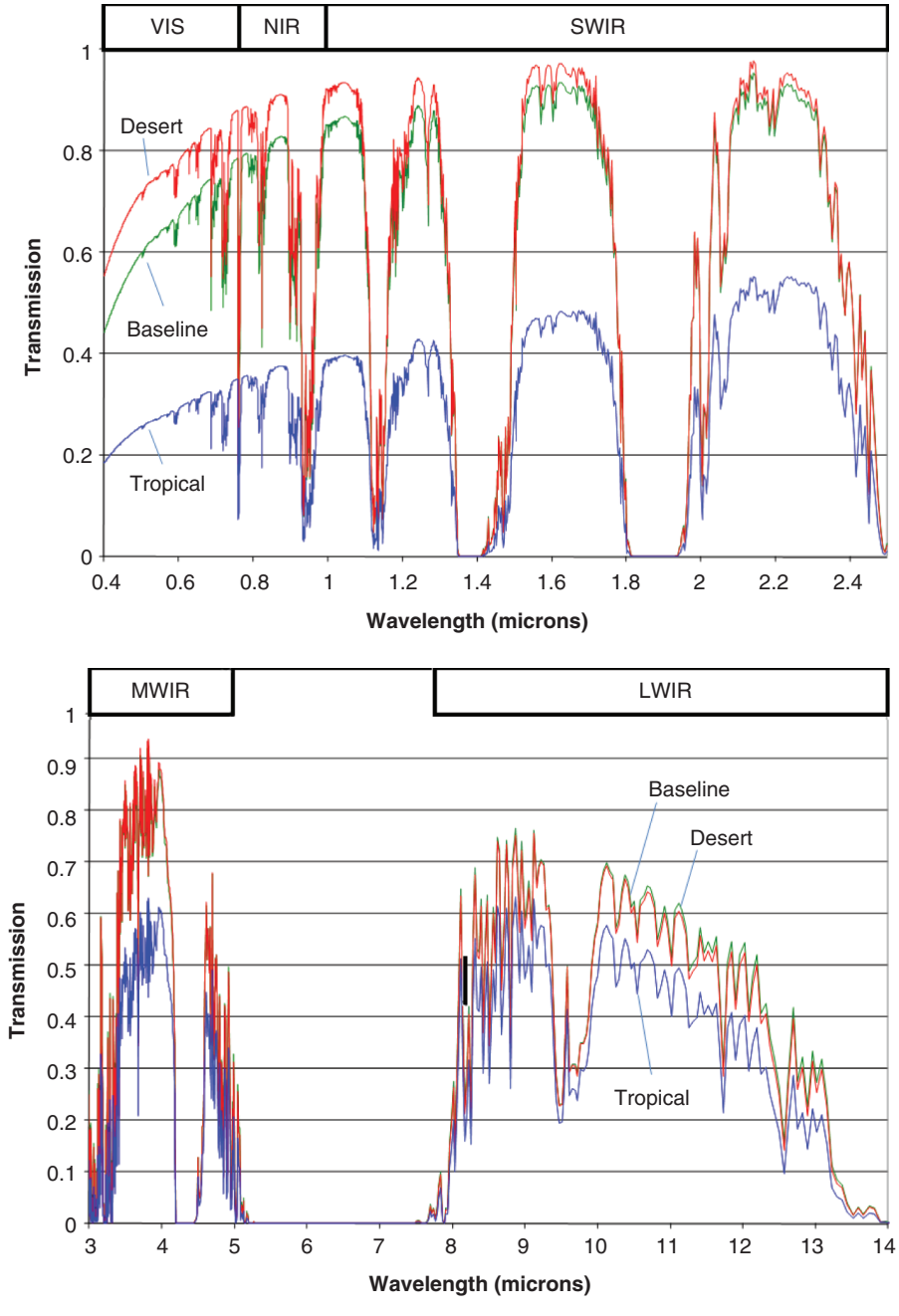

Figure 17.11 (Plate 29) Ground to space atmospheric transmission windows. *See plate section for the color version*

to space transmission over a vertical path in both the reflective (0.4–2.5 μm) and emissive (3–14 μm) spectral regions for some nominal meteorological conditions [27]. The various visible, near infrared (NIR), short-wave infrared (SWIR), mid-wave infrared (MWIR), and long-wave (LWIR) spectral windows are depicted in the transmission plots.

17.4.1 Reflective Bands

In the visible, NIR, and SWIR bands, the atmosphere contributes to the apparent polarization signature in the following ways:

1. solar illumination is absorbed or scattered before reaching the target,
2. target reflected photons are scattered out of the path or absorbed,
3. photons reflected from the target surroundings are scattered into the path,
4. photons from the Sun are scattered into the path.

Scattering has a substantial impact on polarization sensing through an atmospheric path. Scattering models are typically based on Mie calculations [28] from empirical measurements of the compositional characteristics and size distributions of scattering media at various altitudes, and are often characterized in terms of their scattering coefficient and phase function, both of which can be highly wavelength dependent. Figure 17.12 provides the spectral distribution of some example scattering coefficients at two altitudes for mid-latitude summer, 23 km visibility, rural scattering conditions based on the MODTRAN scattering database. In the reflective spectral region, the strong wavelength dependence of the Rayleigh scattering component is evident. At longer wavelengths, the scattering coefficients are lower and exhibit a resonance near 9 μm as the wavelength matches the peak in the size distribution of the larger but less concentrated aerosol particulates. The phase function is modeled by a Henyey–Greenstein function based on an asymmetry parameter that varies somewhat modestly with altitude and conditions.

Rayleigh scattering creates a strong band of polarized sky radiance. The Mueller matrix for Rayleigh scattering [20] is given by

$$M_{ray} = K \begin{bmatrix} 1+\cos^2\theta & -\sin^2\theta & 0 & 0 \\ -\sin^2\theta & 1+\cos^2\theta & 0 & 0 \\ 0 & 0 & 2\cos\theta & 0 \\ 0 & 0 & 0 & 2\cos\theta \end{bmatrix} \tag{17.39}$$

where, in this case, angle θ is defined with respect to the direction of propagation prior to the scattering event. The scattering parameter, K, defines the strength of the scattering interaction and scales with wavelength by λ^{-4}. Scattering Mueller matrices are defined in reference to a plane which contains both the incident and scattered light directions. By convention, polarization in this plane is taken to be the positive S_1 direction [23]. When unpolarized light (such as light from the Sun) is Rayleigh scattered, peak polarization occurs at $\theta = 90^0$ and is oriented perpendicularly to the scattering plane (i.e., $-S_1$ direction). Under clear sky conditions, a band of sky polarization builds up around this peak as shown in Fig. 17.13. (The dark band across this image is the sun occulter. The white regions immediately around the sun are due to image

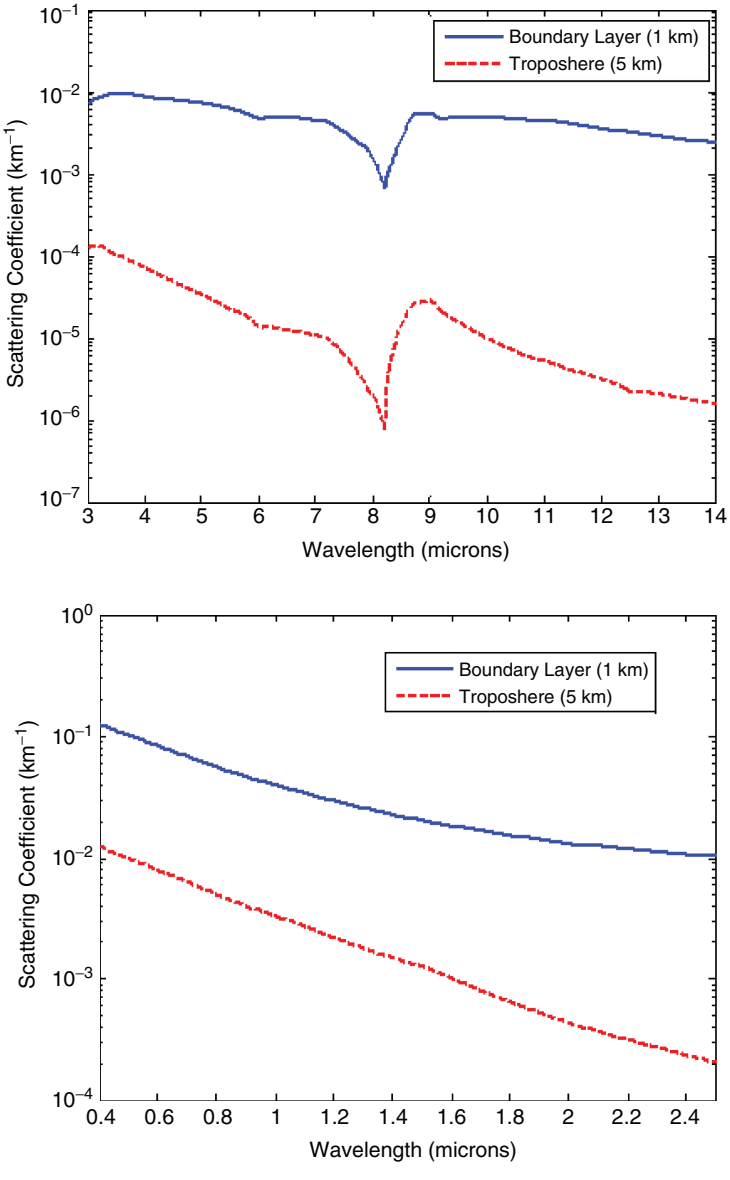

Figure 17.12 Scattering coefficients as a function of altitude at various wavelengths. Note the scale change between plots

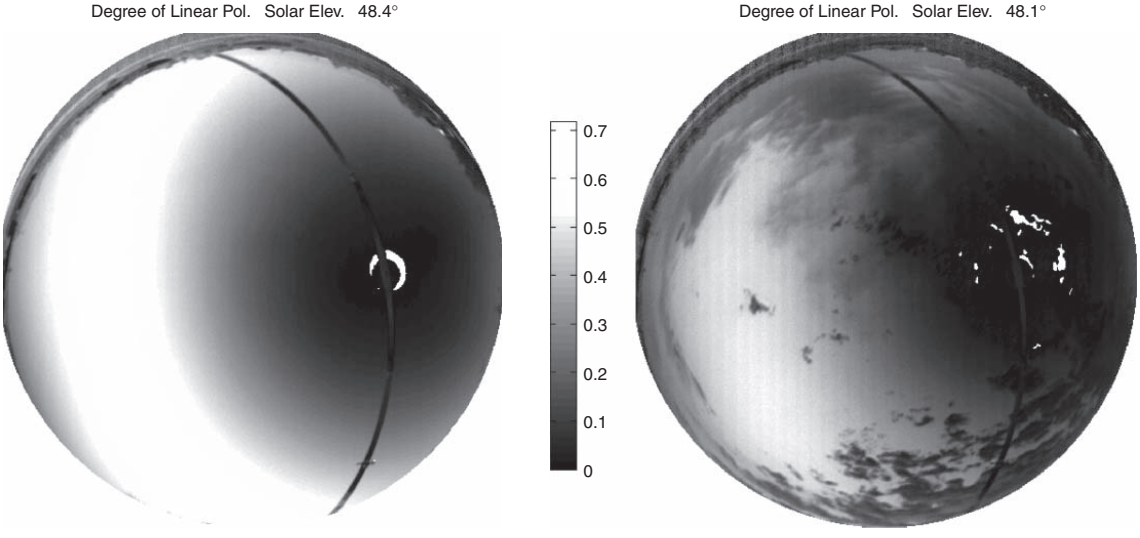

Figure 17.13 Full-sky polarization images at 450 nm: clear skies (*left*) and cloudy skies (*right*) above Montana State University in June, 2012. *Source*: Courtesy of Professor. J. Shaw and Dr. N. Pust, Montana State University

saturation, not actual sky polarization.) Multiple scattering events, each with a different scattering plane, collude to reduce the apparent sky polarization at the ground to something less than the Rayleigh peak (around 70% in this case).

The overall effect of sky polarization will vary depending on the sun-target-sensor geometry. In [29], for a diffuse painted metal target looking generally toward the specular direction of the Sun, direct solar illumination dominated the S_1 signature while the Sun is high but clear sky Rayleigh scattering dominated near sunrise and sunset when the specular contribution of the Sun is weakest. Results for S_2 were less conclusive due to complicating factors. For a more specular target, the duration of solar dominance will be reduced. In cases where there is no direct solar illumination, such as targets in shadows [30], sky/Rayleigh scattering polarization will play a significant role throughout the day.

A pure Rayleigh scattering model is only valid in cases where the scatterers are isotropic and much smaller than λ. Experimental evidence shows that the composition of clouds, aerosols, and surface reflectance all contribute significantly to the polarization character of the sky [31, 32]. Examples of sky polarization under the influence of these complicating factors is shown as measured in Fig. 17.13 (*right*) for clouds and Fig. 17.14 from a validated clear sky model that includes aerosol and ground reflection effects [33].

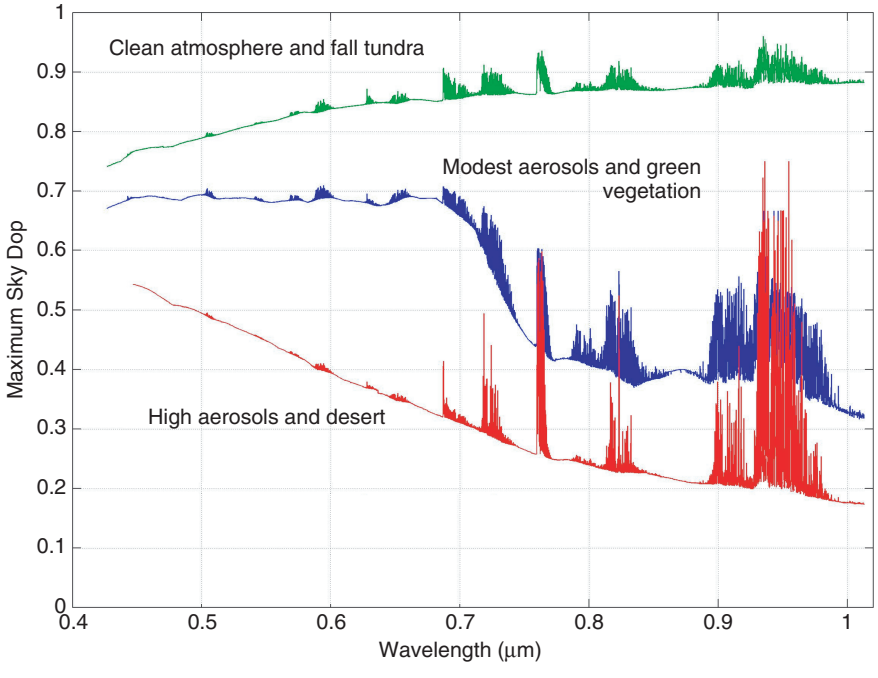

Figure 17.14 Examples of peak sky polarization calculated for various measured aerosol and background conditions in [31]. *Source*: Courtesy of Professor. J. Shaw and Dr. N. Pust, Montana State University

Figure 17.12 suggests diminished sky polarization in the SWIR band. On a clear day, SWIR sky polarization will follow the banding pattern exhibited at shorter wavelengths but with less overall radiance and degree of polarization. Researchers have reported SWIR (1.54 μm) sky degree of polarization varying between approximately 20 and 38% over a 10.5^o Rayleigh scattering arc in a clear summer sky [34].

17.4.2 Emissive Bands

As wavelength increases in the MWIR and LWIR bands, the driving influence of the atmosphere on polarization signatures shifts from scattering to emission. Referring back to Fig. 17.12, the continued overall decline in scattering throughout these bands is evident. In addition to the lingering effects of scattering, the atmosphere affects apparent target signatures through emission of randomly polarized light in the following ways:

1. target reflection of atmospheric emissions and clouds,
2. emission along the path.

In the first case, atmospheric emissions are effectively unpolarized but this radiation becomes partially polarized upon reflection. The reflected light is s-polarized (parallel to the surface) and adds incoherently to the p-polarized (perpendicular to the surface) emission. The combination of s and p polarized radiation results in a reduced apparent degree of polarization. This is part of the reason why humidity is major source of polarization signature variability, especially in the LWIR band (water vapor content also affects absorption). These interactions and others were modeled [35] and measured [36] in detail by Shaw for the case of water bodies.

The role of clouds is highly variable in the emissive bands. In addition to acting as an illumination source for target reflected photons (as discussed previously), clouds also affect the rates of heating and cooling of objects throughout the scene. These combined effects were demonstrated by Felton *et al*. [37] in a study of MWIR and LWIR polarization contrast over several diurnal cycles. They found that LWIR S_1 contrast for a tank hull target is reduced in the presence of clouds but MWIR S_1 increases under the same conditions. LWIR S_1 contrast was reduced to the noise level under totally overcast conditions. In this test, the tank hull temperature was allowed to float with the air temperature. If the tank were operating then the heated surfaces would likely show additional thermal and polarization contrast.

Emission along the path is randomly polarized and will reduce the apparent degree of polarization of the sensed radiation. While the contribution of path emission is insignificant over short distances, it can be fairly substantial over longer propagation paths. Figure 17.15 (Plate 30) illustrates the path radiance over the 3 to 14 μm spectral range over a zenith ground-to-space path for three meteorological conditions. The path radiance is compared to 230 K and 280 K blackbody spectral radiance functions to provide a relative sense of the magnitude of the path radiance [27]. For example, the path radiance is on the order of 30% of the sensed radiation at a 10 μm wavelength for this propagation path.

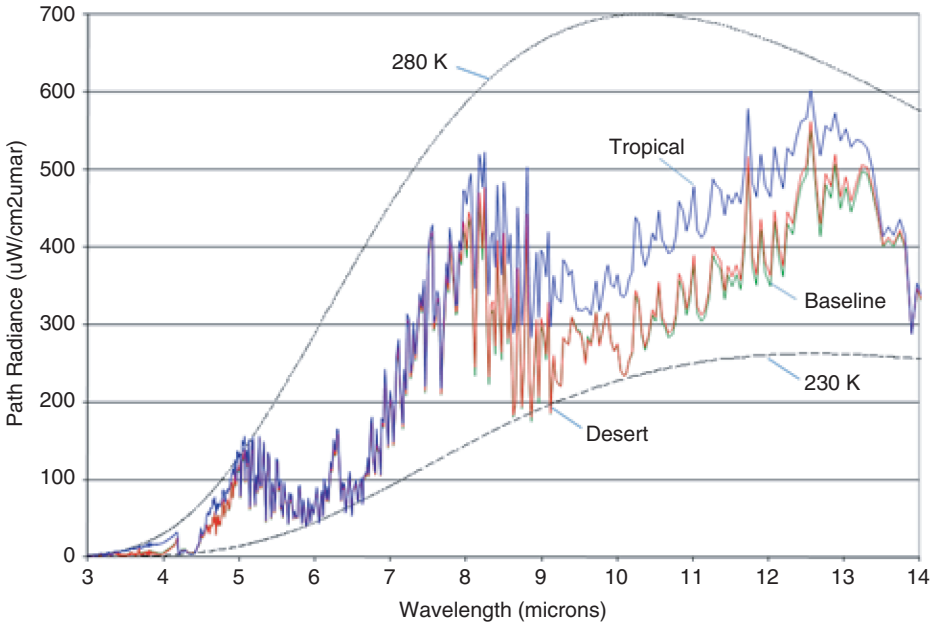

Figure 17.15 (Plate 30) Examples of path emission along a ground to space line of sight as a function of range and atmospheric conditions. *See plate section for the color version*

17.5 Data Reduction Matrix Analysis of Modulated Polarimeters

17.5.1 Important Equations

The *Data Reduction Matrix* (DRM) [18] is a tool for mapping radiometrically calibrated measurements from a polarimeter into Stokes parameters. The DRM is also a tool for modeling calibration errors and choosing optimal sets of measurements. These concepts will be introduced briefly and then applied to the analysis of real systems. For an imaging system, there may be a single DRM for all detectors or it may vary between detector elements. The spatial variability of the DRM will also be addressed in the examples.

Radiation described by Stokes vector $\mathbf{S}$ is incident upon a polarization analyzer defined by Mueller matrix $\boldsymbol{M}_i$. After passing through the analyzer, the following relationship holds between the measured signal I_i and the incident Stokes vector:

$$I_i = \mathbf{A}_i\mathbf{S} + n_i \tag{17.40}$$

$\mathbf{A}_i$ is a row vector given by the first row of $\boldsymbol{M}_i$ and n_i is noise in the measurement. Recall that the first row of $\boldsymbol{M}_i$ maps the incident Stokes vector into the total irradiance on the detector. For N measurements arranged in a vector $\mathbf{I}$, a polarimeter measurement matrix is defined as

$$\boldsymbol{W} = \begin{bmatrix} \mathbf{A}_1 \\ \vdots \\ \mathbf{A}_N \end{bmatrix} \tag{17.41}$$

and the least-squares estimate of $\mathbf{S}$ is

$$\hat{\mathbf{S}} = \boldsymbol{W}^{+}\mathbf{I} \tag{17.42}$$

where the data reduction matrix, $\boldsymbol{W}^{+}$, is the pseudo-inverse of $\boldsymbol{W}$. When $\boldsymbol{W}$ is overdetermined, that is, when there are more irradiance measurements than Stokes parameters, the Moore–Penrose pseudo-inverse is

$$\boldsymbol{W}^{+} = \left(\boldsymbol{W}^{T}\boldsymbol{W}\right)^{-1}\boldsymbol{W}^{T}. \tag{17.43}$$

In an optimal configuration (described next), $\boldsymbol{W}^{T}\boldsymbol{W}$ is a diagonal matrix that makes this pseudoinverse calculation straightforward.

Stokes reconstruction errors occur because of noise and calibration errors in the data reduction matrix [38, 39]. The reconstruction error is the difference between the estimated and measured Stokes vectors

$$\boldsymbol{\epsilon} = \hat{\mathbf{S}} - \mathbf{S}. \tag{17.44}$$

For noise, the error is simply

$$\boldsymbol{\epsilon} = \boldsymbol{W}^{+}\mathbf{n} \tag{17.45}$$

where $\mathbf{n}$ is the vector of noise samples. This type of error is minimized by minimizing the condition number of $\boldsymbol{W}$. For calibration matrix errors of the form,

$$\boldsymbol{W}_{error} = \boldsymbol{W} + \boldsymbol{\Delta} \tag{17.46}$$

the Stokes reconstruction error is

$$\boldsymbol{\epsilon} = \boldsymbol{W}^{+}\boldsymbol{\Delta}\mathbf{S}. \tag{17.47}$$

In these two equations, $\boldsymbol{W}$ is the true calibration matrix and Δ is an additive offset containing all of the calibration error terms. For calibration errors, the total Stokes reconstruction error depends on the input polarization state.

17.5.2 Example Stokes Polarimeters

The work of the last few sections can be brought together through a series of examples. A straightforward implementation of a full Stokes polarimeter consisting of a fixed analyzer (linear diattenuator) and a rotating retarder is shown in Fig. 17.16.

The Mueller matrix of this system is given by

$$\boldsymbol{M}(\theta, \delta) = \boldsymbol{M}_D(p_h, p_v)\boldsymbol{M}_R(-\theta)\boldsymbol{M}_W(\delta)\boldsymbol{M}_R(\theta) \tag{17.48}$$

and the i^{th} measurement vector is given by

$$\mathbf{A}_i = \frac{1}{2}\left[1 \;\; \cos^2 2\theta_i + \cos\delta \sin^2 2\theta_i \;\; (1-\cos\delta)\cos 2\theta_i \sin 2\theta_i \;\; -\sin\delta \sin 2\theta_i\right] \tag{17.49}$$

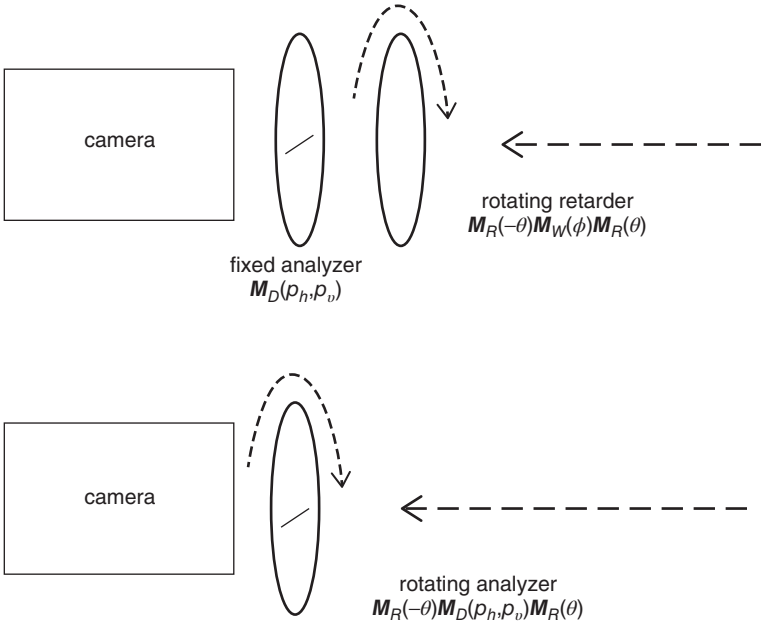

Figure 17.16 Diagrams of the rotating retarder (*top*) and rotating analyzer (*bottom*) polarimeters

for the case where the diattenuator is ideal with a horizontal preference for transmission ($p_h = 1$ and $p_v = 0$). The rotating retarder polarimeter can be analyzed on the Poincaré sphere. Figure 17.17 illustrates how choice of retardance, δ, affects the analyzer states available to the polarimeter. Each plotted point corresponds to the Stokes vector that is transmitted with maximum irradiance through the system at retarder orientation angle θ_i as it rotates through 180^o. In the $\delta = 90^o$ case, the curve has components along each of the Stokes parameter directions. Consequently, there are many possible combinations of measurements made along this curve that will result in reconstruction of the full Stokes vector using Eq. 17.42. On the other hand, the $\delta = 180^o$ curve has zero length in the S_3 direction for all θ_i and there is no measurement combination that will result in reconstruction of S_3.

Clearly, some choices of δ are superior to others if reconstruction of the full Stokes vector is the goal. After δ is selected, some set of retarder orientation angles must also be selected to build up $\boldsymbol{W}$. The best choices will be those that minimize errors in the presence of noise across the reconstructed Stokes parameters. This minimum error situation is found by selecting the retardance and measurement orientation angles that minimize the Frobenius norm condition number of $\boldsymbol{W}$

$$c = \|\boldsymbol{W}\|_F \|\boldsymbol{W}^+\|_F \tag{17.50}$$

such that

$$\|\boldsymbol{W}\|_F = \sqrt{\sum_{i=1}^{m}\sum_{j=1}^{n} |w_{ij}|^2} \tag{17.51}$$

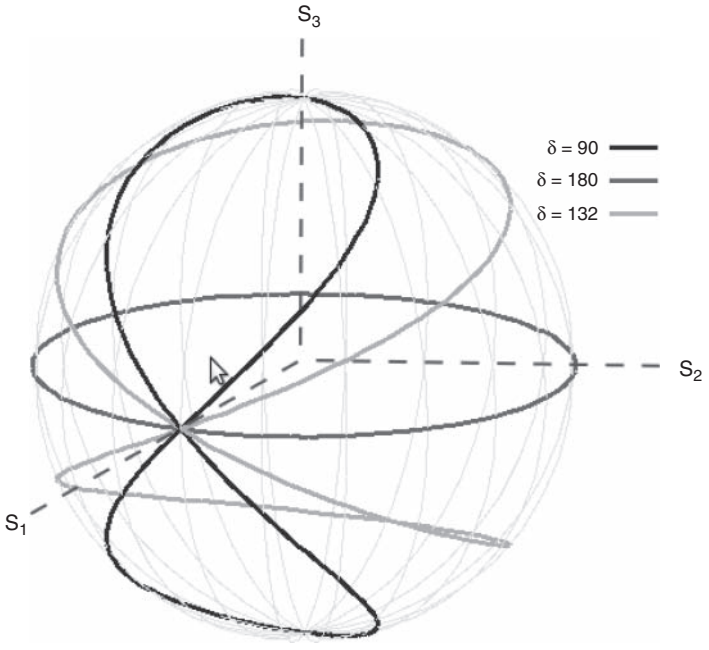

Figure 17.17 Variations on the rotating retarder polarimeter plotted on the Poincaré sphere

where $\boldsymbol{W}$ is taken to be an $m \times n$ matrix with elements w_{ij}. In [40] it is shown that the minimum condition number criterion for the rotating retarder polarimeter is achieved at $\delta = 132°$ (this curve is also shown in Fig. 17.17). Assuming four measurements are made to retrieve each Stokes vector, the optimal values for θ_i are $\pm 15.1^{\circ}$ and $\pm 51.6^{\circ}$.

As shown in Section 17.3, little is sacrificed by ignoring S_3 in passive polarimetric imaging. For this reason, linear Stokes polarimeters, that is, systems that determine S_0, S_1, and S_2 exclusively, are in widespread use. The rotating retarder polarimeter with $\delta = 180^{o}$ is one example of a linear Stokes polarimeter that comes with several advantages but large broadband retarders are expensive in the infrared bands. An alternative way of constructing such a system is to place a rotating linear diattenuator/analyzer at the aperture of the imaging system as show in Figure 17.16 (*bottom*). For this rotating analyzer case, the throughput of the system is sensitive to the Mueller matrix of the optics between the analyzer and the detector array. A procedure for including the polarizing effects of the focusing optics will be presented in Section 17.7.

Both the rotating retarder and rotating analyzer schemes are examples of *division-of-time* (DoT) polarimeters. Another option is to spatially vary the measurement analyzers in a repeating pattern at the detector level as shown in Fig. 17.18. This is called a division-of-focal plane (DoFP) or micrograd polarimeter. The term "micrograd" refers to the wire grid polarizers that are bonded to the detector array to achieve polarization sensitivity.

The following example applies to either rotating analyzer or micrograd imaging polarimeters. In the rotating analyzer case, the full DRM is built up over time for every pixel. For micrograd systems, the DRM at each pixel can be built up simultaneously after some form of interpolation

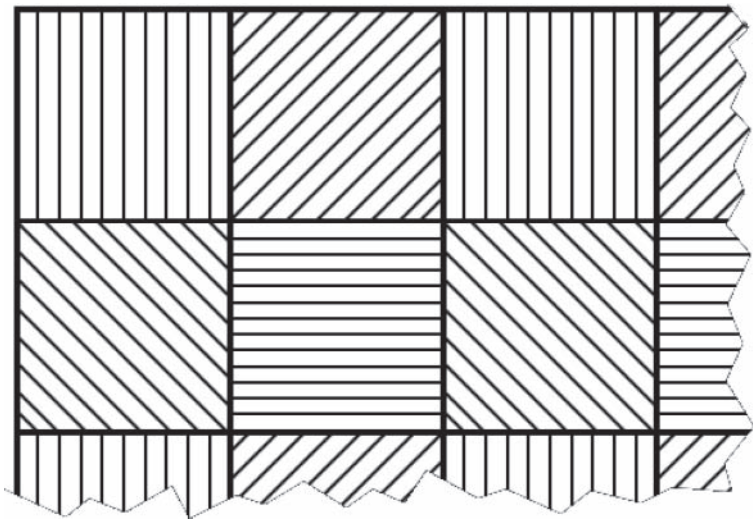

Figure 17.18 A microgrid polarizer array. Thin lines represent direction of the thin wires that prevent light polarized in this direction to pass

using adjacent pixels (however, a better option will be discussed in Section 17.6). The Mueller matrix for this imaging system is given by:

$$\boldsymbol{M}(\theta) = \boldsymbol{M}_R(-\theta)\boldsymbol{M}_D(p_h, p_v)\boldsymbol{M}_R(\theta). \tag{17.52}$$

For the sake of simplicity, the Mueller matrix of the focusing optics for this imaging system is assumed to be the identity matrix. The resulting analyzer vector is:

$$\mathbf{A}_i = \frac{1}{2}\left[p_h^2 + p_v^2 \;\; (p_h^2 - p_v^2)\cos 2\theta_i \;\; (p_h^2 - p_v^2)\sin 2\theta_i\right] \tag{17.53}$$

This analyzer vector has been truncated to three elements because reconstruction of S_3 is not a concern. Of course, $\mathbf{A}_i$ can now only operate on three element Stokes vectors. The energy in any unaccounted for S_3 component is still retained in S_0. For instance, right-hand circular polarized light would be seen by this polarimeter as unpolarized light whether or not there is a zero-valued fourth element in this analyzer vector. This simplification sacrifices nothing and will make calculation of the DRM easier later on.

To find three Stokes parameters, the number of measurements N must be greater than or equal to 3. The analyzer orientation angles are selected to minimize the condition number of $\boldsymbol{W}$ thereby optimizing performance in the presence of noise. The current system is only sensitive to linear polarization states so the minimum condition number is found by spreading the choices for θ_i out evenly over all possible values of the orientation angle ψ. For instance, for a three measurement system, the separation between each θ_i should be 60°. For a four channel system (like the microgrid case), this spacing is 45°. In practice, more that three rotating analyzer measurements may be made to reduce noise. Each of these configurations have a condition number of $\sqrt{2}$.

The example of the four channel linear Stokes polarimeter is useful because it can represent either the microgrid or rotating analyzer cases and the pseudoinverse of $\boldsymbol{W}$ may be calculated by hand. The analyzer angles are optimally spaced at 0, 45, 90, and 135 degrees. Without loss of generality, assume that the neutral density transmission loss in the analyzer, $p_h^2 + p_v^2 = 1$. The true transmission loss can be multiplied back in after analysis of the system is complete. The resulting analyzer matrix and DRM are:

$$\boldsymbol{W} = \frac{1}{2}\begin{bmatrix} 1 & D & 0 \\ 1 & 0 & D \\ 1 & -D & 0 \\ 1 & 0 & -D \end{bmatrix} \tag{17.54}$$

$$\boldsymbol{W}^+ = \begin{bmatrix} \frac{1}{2} & \frac{1}{2} & \frac{1}{2} & \frac{1}{2} \\ D^{-1} & 0 & -D^{-1} & 0 \\ 0 & D^{-1} & 0 & -D^{-1} \end{bmatrix} \tag{17.55}$$

where D is the linear diattenuation,

$$D = \frac{p_h^2 - p_v^2}{p_h^2 + p_v^2}. \tag{17.56}$$

Diattenuation expresses how well an analyzer extinguishes light that is polarized perpendicular to its preferred transmission axis. For rotating analyzer systems, diattenuation can be close to 1 (nearly ideal). Microgrid polarimeters have lower effective diattenuation values because of optical (diffraction) and electronic crosstalk between adjacent detectors. The following example examines the effect of diattenuation on Stokes reconstruction errors.

Using Eq. 17.45, the reconstruction error due to noise is

$$\boldsymbol{\epsilon} = \boldsymbol{W}^+\mathbf{n} = \begin{bmatrix} \frac{1}{2}(n_1 + n_2 + n_3 + n_4) \\ D^{-1}(n_1 - n_3) \\ D^{-1}(n_2 - n_4) \end{bmatrix}. \tag{17.57}$$

Thus the reconstruction of S_0 is unaffected by diattenuation but the noise in S_1 and S_2 increases as diattenuation decreases.

If diattenuation is ignored and the analyzers are assumed to be ideal in the calibration matrix then a different kind of Stokes reconstruction error occurs. To find this error, the calibration matrix of the idealized four channel polarimeter ($D = 1$) is decomposed according to Eq. 17.46

$$\boldsymbol{W}_{ideal} = \boldsymbol{W} + \boldsymbol{\Delta} = \frac{1}{2}\begin{bmatrix} 1 & D & 0 \\ 1 & 0 & D \\ 1 & -D & 0 \\ 1 & 0 & -D \end{bmatrix} + \frac{1}{2}\begin{bmatrix} 0 & 1-D & 0 \\ 0 & 0 & 1-D \\ 0 & D-1 & 0 \\ 0 & 0 & D-1 \\ . & & \end{bmatrix}. \tag{17.58}$$

The reconstruction error that results is given by Eq. 17.47,

$$\epsilon = \boldsymbol{W}^+\boldsymbol{\Delta}\mathbf{S} = (D^{-1} - 1)\begin{bmatrix} 0 \\ S_1 \\ S_2 \end{bmatrix}. \tag{17.59}$$

In other words, S_1 and S_2 are overestimated if diattenuation is not included in the DRM. This example is intended to be illustrative but imperfect diattenuation is only one of many ways in which polarimeter calibration may be non-ideal. In general, every optical element in the polarimeter contributes some diattenuation, retardance, depolarization, and misalignment [18].

17.6 Fourier Domain Analysis of Modulated Polarimeters

The applications of imaging polarimetry include many cases where the intended target varies appreciably (temporally and/or spatially) during the measurement interval. The purpose of this section is to address Stokes reconstruction for dynamic scenes. This discussion will unfold via the examples of the rotating analyzer and microgrid polarimeters described in Section 17.5. The tools developed below may then be readily extended by the reader to other modulated polarimeter designs.

17.6.1 Rotating Analyzer

The analyzer vector of the rotating analyzer polarimeter is described by Eq. 17.53. Assume ideal polarization optics, that is, $D = 1$. From Eq. 17.40, the irradiance at an arbitrary detector at time t is given by

$$I(t) = \frac{1}{2}[S_0(t) + S_1(t)\cos 2\theta(t) + S_2(t)\sin 2\theta(t)]. \tag{17.60}$$

As the analyzer rotates,

$$\theta(t) = 2\pi f_R t \tag{17.61}$$

where f_R is the rotation frequency of the analyzer. The detector array samples this signal with frequency f_S which is assumed to be greater than f_R. To avoid unnecessary details, the sample duration is taken to be effectively instantaneous and $I(t)$ is bandlimited. The n^{th} sample of this signal is

$$I(n) = \frac{1}{2}[S_0(n) + S_1(n)\cos(\alpha n) + S_2(n)\sin(\alpha n)] \tag{17.62}$$

where

$$\alpha = 4\pi\frac{f_R}{f_S} \tag{17.63}$$

and the *Discrete-Time Fourier Transform* (DTFT) of 17.62 is,

$$\tilde{I}(\omega) = \frac{1}{2}\left\{\tilde{S}_0(\omega) + \pi\delta(\omega-\alpha)\left[\tilde{S}_1(\omega) + i\tilde{S}_2(\omega)\right] + \pi\delta(\omega+\alpha)\left[\tilde{S}_1(\omega) - i\tilde{S}_2(\omega)\right]\right\} \tag{17.64}$$

where ω is the angular frequency.

As a brief review, the DTFT is periodic over increments of 2π radians. Integer multiples of the folding frequency, $\omega = \pi$, correspond to the maximum analog frequency, $f_S/2$, that may be accurately reconstructed by the sampled data ($f_S/2$ is also referred to as the Nyquist frequency). Spectral content beyond the Nyquist frequency is aliased into lower frequency portions of the spectrum resulting in undesirable artifacts in the reconstructed data. The S_1 and S_2 components of 17.64, which contain all of the polarization information in the sampled signal, are modulated

out to a $\pm\alpha$ sideband while the total intensity component, S_0, is the baseband. Spectral content near the center of the baseband and sidebands represent signal components that vary relatively slowly while more rapid signal variations are captured at frequencies away from the band centers.

The frequency range occupied by the signal is referred to as its bandwidth. A sketch of the magnitude of this spectrum when sampled for maximum available bandwidth is shown in Fig. 17.19. It is possible that the bandwidth of the S_0 component will be different than the S_1 and S_2 bandwidths. To guarantee that a signal with analog bandwidth B can be reconstructed properly,

$$\frac{2\pi}{f_S}B \leq \alpha \tag{17.65}$$

and

$$3\alpha \leq 2\pi. \tag{17.66}$$

Together, these requirements ensure that three full bandwidths (one for the baseband and two for the sidebands) may be contained without overlap within the DTFT spectrum. As shown by [41], these requirements become

$$f_S \geq 6f_R \tag{17.67}$$

and

$$B \leq 2f_R \tag{17.68}$$

One key result of this analysis is that the temporal bandwidth capacity of division-of-time polarimeters is always less than that of the underlying imaging system. In other words, sensitivity to polarization is achieved by sacrificing temporal resolution.

This Fourier analysis also shows how Stokes parameter reconstruction can be viewed as a combination of modulation and low pass filtering operations. The DRM in Section 17.5 represents one particular choice of low pass filter, a rectangular window in time.

17.6.2 Microgrid Polarimeters

Fourier analysis of the microgrid polarimeter was first carried out in [42]. Referring back to Fig. 17.18, each pixel in a raw microgrid intensity image samples a point in the scene as projected through a polarization analyzer. Ideally, the analyzer at each sampling point is identical

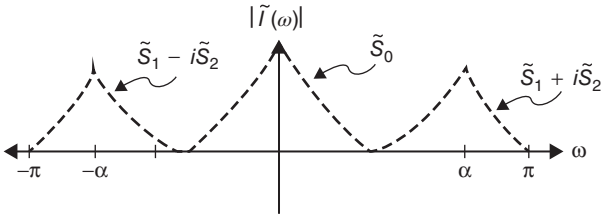

Figure 17.19 Magnitude of the discrete time rotating analyzer spectrum with annotations for the Stokes components

except for rotation in a repeating pattern (0^o, 45^o, 90^o, and 135^o) as shown in Fig. 17.18. The sampled intensity at each point (m, n) in a raw microgrid image is given by

$$\begin{aligned} I(m,n) =& \frac{1}{2}S_0(m,n) + \frac{1}{4}\cos(\pi m)[S_1(m,n) + S_2(m,n)] \\ &+ \frac{1}{4}\cos(\pi n)[S_1(m,n) - S_2(m,n)] \end{aligned} \tag{17.69}$$

where each of the $S_x(m, n)$ terms represent one of the Stokes parameter images as it varies in space. The DSFT of I is given by:

$$\begin{aligned} \tilde{I}(\xi,\eta) =& \frac{1}{2}\tilde{S}_0(\xi,\eta) + \frac{\pi}{4}\left[\tilde{S}_1(\xi-\pi,\eta) + \tilde{S}_2(\xi-\pi,\eta)\right] \\ &+ \frac{\pi}{4}\left[\tilde{S}_1(\xi,\eta-\pi) - \tilde{S}_2(\xi,\eta-\pi)\right] \end{aligned} \tag{17.70}$$

where each of ξ and η are real-valued spatial frequency coordinates defined over one period of the spectrum, that is, $-\pi \leq \xi, \eta \leq \pi$. An illustration of the microgrid DSFT is shown in Fig. 17.20.

Similar to the rotating analyzer case, the S_1 and S_2 components of the microgrid spectrum are modulated out into sidebands while the S_0 signal remains at baseband. Tyo *et al*. [42] established a sufficient condition to avoid aliasing in terms of a band radius in ξ and η space:

$$r_{S_0} + r_{S_1 \pm S_2} < \pi \tag{17.71}$$

where each r_x is the radius, in radians per sample, of the smallest circle that encloses the band limits on S_0 or $S_1 \pm S_2$. In almost every case, the bandwidth occupied by S_0 is larger than the $S_1 \pm S_2$ bandwidth.

This bandwidth condition can be difficult to meet. Given a detector spacing of d_x, the Nyquist frequency of the microgrid imager is

$$f_x = \frac{1}{2d_x} \tag{17.72}$$

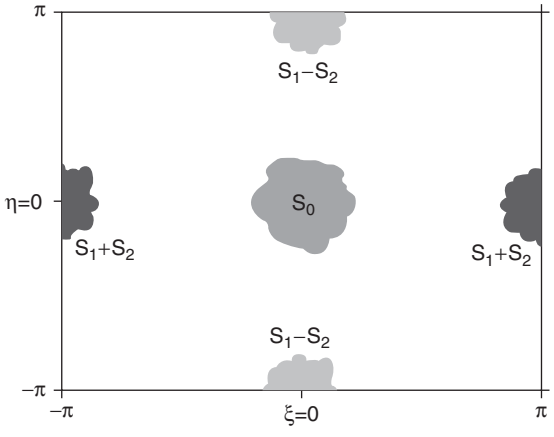

Figure 17.20 Magnitude of the microgrid analyzer spectrum with annotations for the Stokes components

Note that d_x is the detector spacing, not the spacing between like-oriented analyzer samples. The ultimate limit on the image bandwidth is imposed by the optical system:

$$f_o = \frac{1}{\lambda F_\#} \tag{17.73}$$

where λ is the operating wavelength and $F_\#$ is the f-number of the optical system [43]. If $f_x < f_o$ then aliasing and spectral mixing between the S_0 baseband and the S_1, S_2 sidebands is going to occur. Though detector sizes continue to decrease, aliasing is common problem for microgrid systems in the infrared bands.

Microgrid Stokes image reconstruction under these conditions has been attempted using like-polarization interpolation [44], Fourier domain processing [42, 45], bilateral filtering [46], and multi-frame super-resolution [47].

17.6.3 Band-Limited Stokes Reconstruction

Stokes parameter estimation using the data reduction matrix is highly susceptible to reconstruction errors due to changes in the input signal. In other words, the DRM works best when the signal presented to the aperture is approximately constant. Lacasse *et al.* [41] provide an alternative to the DRM that can exploit time/space varying signals for modulated polarimeters up to the bandwidth limits presented in the previous sections. For a division-of-time polarimeter, the reconstructed Stokes vector at sample n is

$$\hat{\mathbf{S}}(n) = \mathbf{Z}^{-1}(n)\left[w * \mathbf{A}^T I\right](n) \tag{17.74}$$

where

$$\mathbf{Z}(n) = \left[w * \mathbf{A}^T \mathbf{A}\right](n). \tag{17.75}$$

In these equations, $w(n)$ is a filter window; $\mathbf{A}(n)$ is the analyzer row vector at this reconstruction location; $I(n)$ is the measured irradiance; and $*$ is the discrete convolution operator. The window function is the low pass filter used to weight the measurements contributing to the Stokes reconstruction at n. Matrix $\mathbf{Z}(n)$ separates out the Stokes parameters from the products of the demodulation process in $[w * \mathbf{A}^T I](n)$.

Equation 17.74 is equivalent to the traditional DRM when the window function, $w(n)$, is rectangular [48]

$$w_r(n) = \begin{cases} 1 & \text{if} \quad n < N-1 \\ 0 & \text{otherwise.} \end{cases} \tag{17.76}$$

The length, N, of the reconstruction window determines how fast the polarimeter responds to signal variations, how accurately the signal will be reconstructed, and how much cross-spectral contamination there will be between the baseband and sidebands in the reconstruction process. As an example, Fig. 17.21 shows the filter response for two different rectangular windows applied to a rotating analyzer polarimeter that has been sampled according to Eqs. 17.67 and 17.68. The three sample window has a broad frequency response but it also has a significant response outside of the maximum available reconstruction bandwidth. Except for the case of a constant signal (where the signal spectrum consists of delta functions at 0 and $\pm\alpha$ radians/sample), this filter guarantees some cross-spectral contamination. When the window is made

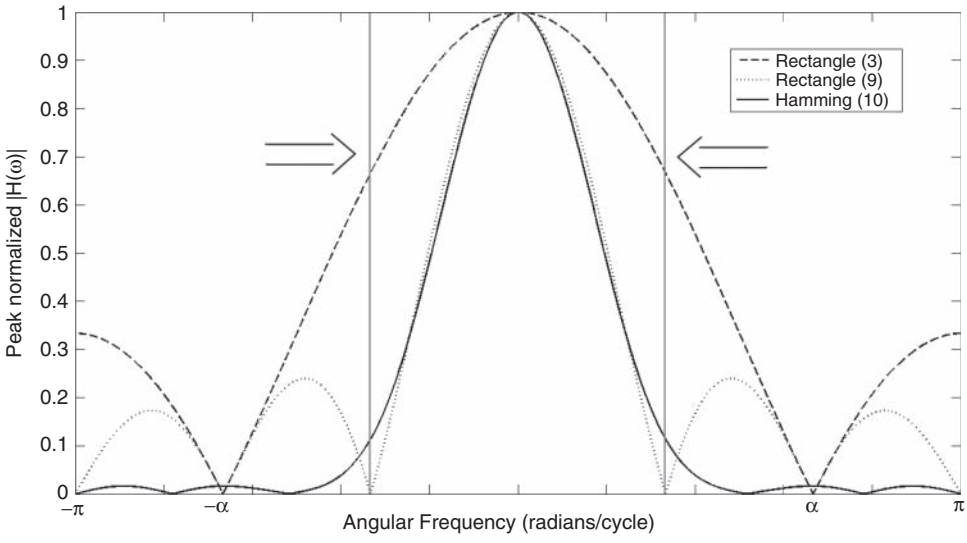

Figure 17.21 Frequency response to various Rotating Analyzer polarimeter reconstruction filters. Maximum reconstruction bandwidth is indicated by arrows on the figure

three times longer, this out of band response is diminished at the cost of diminished high frequency response *within* the passband.

Equation 17.74 allows the reconstruction window to be tailored for improved performance. For real-time systems, a Hamming window is one option that offers an improvement over the rectangular DRM window. The Hamming window of length N is

$$w_h(n) = a - (1 - a) * \cos\left(\frac{2\pi(n)}{N - 1}\right) \tag{17.77}$$

where $a = 0.54$. A 10 sample Hamming window is also shown in Fig. 17.21. It has an in-band frequency response that is almost identical to the nine sample rectangle window while providing nearly complete out of band rejection.

It is also possible to approximate a filter with DSFT bandwidth α and unit magnitude inside the pass-band (i.e., a rectangular frequency response) using a truncated sinc style window. However, this window will result in substantial reconstruction artifacts if the input measurements are not truly band-limited, which is often the case in real systems.

In the example here, n is a one-dimensional series of samples in a division-of-time polarimeter but this method extends readily to the two-dimensional microgrid case. Unlike the methods listed at the end of Section 17.6.2, this method also allows for non-ideal and spatially varying analyzer vectors.

17.7 Radiometric and Polarimetric Calibration

Reliable imaging polarimetry requires sensor calibration. This calibration is composed of two parts: a mapping of sensor digital counts into radiometric units and then an accurate mapping

of radiometric values into polarimetric quantities. The procedures for conducting radiometric and polarimetric calibration are described in this section.

17.7.1 Radiometric Non-Uniformity Correction

Each detector in an infrared imaging array responds to the arrival of photons in a slightly different way. Read-out electronics also affect how this detected signal is interpreted and recorded. Additionally, vignetting may affect apparent scene radiance at the edge of the image even in well-designed optical systems. These non-uniformities in detector and read-out response degrade the image on both small (e.g., pixel by pixel) and large (rows or regions of pixels) scales. The polarimetric data reduction matrix makes no accommodation for this issue and, therefore, these detector variations must be eliminated as a preprocessing step.

For InSb and HgCdTe imaging arrays, $L(x, y)$, the radiometrically corrected response for a detector in array position (x, y), is well modeled as using a piecewise linear fit. For imaging polarimeters without rotating optics, this relationship is given by

$$L(x, y) = m_j(x, y)C(x, y) + b_j(x, y) \tag{17.78}$$

where $C(x, y)$ is the raw digital counts from the camera, $m_j(x, y)$ is the slope of the detector response and $b_j(x, y)$ is the offset. The subscript j represents the subrange of count values over which each b_j and m_j are valid. These subranges are generally set globally for the entire array. The width of these subranges must be established experimentally. Each pair of b_j and m_j are readily determined by recording the response of the system at a minimum of two known radiometric levels within each count subrange and then solving the resulting system of equations. In general, a new set of calibration coefficients is required whenever the camera is turned off, when integration time or gain is changed, or after the camera response drifts during periods of extended use.

For imaging polarimeters with moving parts, a radiometric calibration is also required at each analyzer position. In this case,

$$L(x, y) = m_{ij}(x, y)C(x, y) + b_{ij}(x, y) \tag{17.79}$$

where the additional subscript i now corresponds to the analyzer orientation $\boldsymbol{\theta}_i$.

For imagers in the MWIR and LWIR atmospheric transmission bands, a blackbody radiator is used for radiometric input. At shorter wavelengths, a integrating sphere is often used though other less expensive diffuse sources can be purchased or built. In all cases, the radiating surface must produce uniform radiance over an area at least as large as the aperture of the imager. During calibration, this radiating surface is placed as close the camera aperture as possible.

Detector response will drift during periods of continuous use. Periodic re-calibration is necessary, especially for HgCdTe arrays, which places limits on sensor availability. Radiometric calibration time can be extended significantly through the use of scene-based non-uniformity correction. Two recent papers [49, 50] address this issue specifically for the case of microgrid polarimetric imagery.

17.7.2 Polarimetric Calibration

The purpose of polarimetric calibration is to ensure that the data reduction matrix faithfully reconstructs Stokes vectors throughout the scene. Unlike radiometric calibration, polarimetric calibration is only necessary when some change occurs affecting the optical system. For instance, changes to lenses, bandpass filters, or any of the polarization optics are all reasons to conduct a polarimetric calibration.

Persons, *et al*. [51], describe a laboratory setup for polarization calibration as shown in Fig. 17.22. A transmissive polarization target is placed in front of an incoherent illumination source so that it can be imaged by the camera under test. The target is designed so that the transmitted Stokes vector can be changed according to the needs of the test. The polarization target is tilted slightly so that stray light reflected from its surface and into the camera is held fixed by an external reference. After setup is complete, the data collection proceeds as follows

1. The illumination source is set to temperature T_1
2. Measurements $m = 1$ to M are made
   (a) The polarization reference is set to generate Stokes vector $\mathbf{S}_m(T_x)$
   (b) The camera records the response vector $\mathbf{L}_m(T_x)$. The response vector consists of radiance measurements from each analyzer state
3. The illumination source is set to temperature T_2
4. Step 2 is repeated

The estimate of the measurement matrix, $\hat{\mathbf{W}}$, is then given by

$$\hat{\mathbf{W}} = [\boldsymbol{L}(T_1) - \boldsymbol{L}(T_2)][\boldsymbol{S}(T_1) - \boldsymbol{S}(T_2)]^{+} \tag{17.80}$$

where

$$\boldsymbol{S}(T_{\mathrm{x}}) = \left[\mathbf{S}_1(T_{\mathrm{x}}) \ \ldots \ \mathbf{S}_M(T_{\mathrm{x}})\right] \tag{17.81}$$

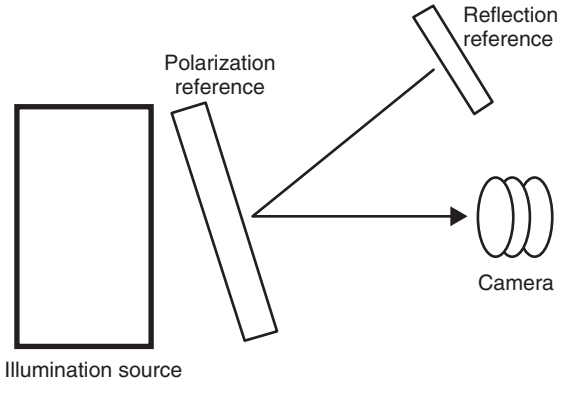

Figure 17.22 Laboratory setup for polarization calibration

and

$$\boldsymbol{L}(T_{\mathrm{x}}) = \left[\mathbf{L}_1(T_{\mathrm{x}}) \ \ldots \ \mathbf{L}_M(T_{\mathrm{x}})\right]. \tag{17.82}$$

The purpose of the signal subtraction (and of using the reflection reference) is to remove any unmodeled contributions from polarization target emission or reflections from the target's surroundings.

Obviously, this calibration procedure is only valid if the Stokes vectors produced by the polarization reference are known precisely, at least to a constant radiometric scale factor. As an example, the polarization reference for calibrating a linear Stokes polarimeter may be a rotating polarizer (linear diattenuator) in a rotation stage. The diattenuation of this device (see Eq. 17.56) must be taken into account. Additionally, the spectral content of the illumination source should be consistent with real-world operations. For polarimetric imagers in the emissive bands, the reference source is a blackbody operated at temperatures inside of the camera's radiometric range. It should be clear from the discussion in Section 17.5 that the Stokes vectors in Eq. 17.81 should be spread out as far apart as possible on the accessible parts Poincaré sphere.

17.8 Polarimetric Target Detection

Sometimes it is desired to accentuate objects in a scene that are anomalous to the Stokes image background. We refer to these objects of interest as targets, and this process of accentuating them as target detection. The optimum detection strategy is the Neyman–Pearson test that forms a detection statistic as a likelihood ratio of an alternative (target present) hypothesis and a null (target absent) hypothesis [52]. These likelihood functions represent the known or assumed statistical models for the target and background. In an anomaly detector, no information is known or assumed for the target, and the detector is completely specified by the statistical model of the background. A common model for vector data is the multivariate normal model, which leads to the Mahalanobis distance or multivariate energy detector. This, however, is not usually a good choice for multispectral or polarimetric imagery because the background is non-stationary and not well represented by global normal statistics.

To address the non-stationarity problem associated with multivariate imagery, Reed and (Xiaoli) Yu developed a spatially adaptive anomaly detector based on local normal statistics that has exhibited good performance for multispectral imaging sensors [53]. This RX algorithm forms a pixel-by-pixel detection statistic given by

$$r(\mathbf{x}) = (\mathbf{x} - \mathbf{m}_b)^T \boldsymbol{C}_b^{-1} (\mathbf{x} - \mathbf{m}_b) \tag{17.83}$$

where $\mathbf{x}$ is the vector data for the pixel under test (or sample mean over a target region), $\mathbf{m}_b$ is the local sample mean vector for a background region around the pixel under test, and $\boldsymbol{C}_b$ is the local sample covariance matrix for the background region as depicted in Fig. 17.23. The size of the target region is selected to match the expected target size, and the size of the background region is a compromise between covariance matrix estimation accuracy (large region) and spatial adaptivity (small region). Sometimes a guard region is placed around the target region to avoid corrupting the covariance matrix with target data. As the pixel under

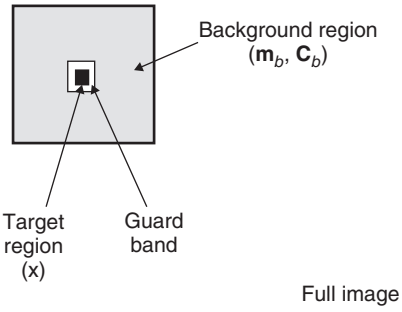

Figure 17.23 Regions of interest in the RX algorithm

test moves across the image, the local target mean vector and background covariance matrix need to be recomputed, producing a computational cost to the spatial adaptivity. Targets are detected by thresholding the detection statistic at a level that provides the desired false alarm rate. Pixels with detection statistic values above threshold are declared as targets.

The benefit of the spatial adaptivity of the RX algorithm is that it supports good detection performance even in the presence of inhomogeneous background clutter, which is very important when applied to multispectral imagery. When applied to polarimetric imagery, this spatial adaptivity might not seem as important for the theoretical case in which the background is truly unpolarized. In this case, the target can be detected simply by thresholding the degree of polarization image. However, there can be polarized content in the background clutter, or even variations in the S_1 and S_2 Stokes images due to miscalibration and other sensor artifacts, that result in inhomogeneous clutter in these components. In such cases, one can use the RX algorithm simply by defining $\mathbf{x}$ in the detection statistic as the entire Stokes vector or the two linear components depending on what target characteristics are considered anomalous. If the entire Stokes vector is used, the algorithm will detect objects that are anomalously intense or polarized. By removing the S_0 component in the RX implementation, the influence of intensity is removed.

As an example, the RX algorithm was applied to the polarimetric dataset in Fig. 17.6 with the results displayed in Fig. 17.24. The image on the left shows the degree of linear polarization, which indicates the highly polarized object, but also shows some variation in the background polarization. The RX algorithm was applied in this case only to the S_1 and S_2 components of the polarimetric image since the S_0 component was so heavily dominated by the background clutter. A single pixel target window was used with a 49×49 pixel background window and 19×19 pixel guard band (nominally the target size). The RX detection statistic image is shown on the right where it is scaled at one-fourth the peak response. In this case, the detection statistic at the center of the target was over a factor of two higher than anywhere else in the image, so the target could be detected with no false alarms if a threshold was used at this level. With the given scaling, it is evident that there are some bright single pixel responses throughout the image that would represent false alarms if not filtered out by either a high enough detection statistic threshold or spatial filtering to remove isolated single-pixel detections.

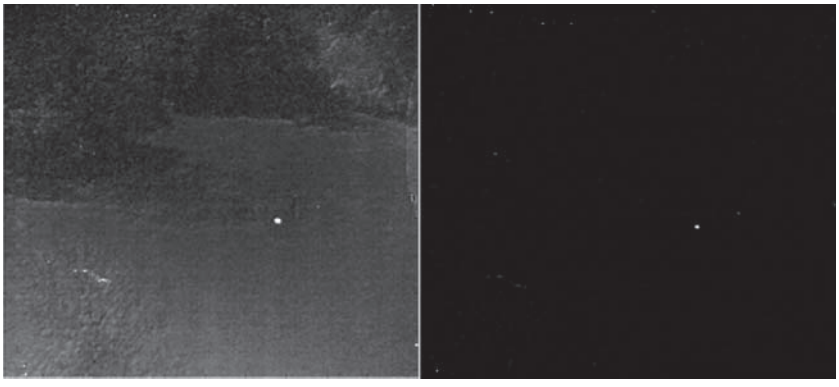

Figure 17.24 Comparison of a DOLP image (*left*) and RX detection map (*right*)

References

[1] Rogne T., F. Smith, and J. Rice, "Passive target detection using polarized components of infrared signatures," *Proceedings of the SPIE 1317*, 1990.

[2] Howe J., M. Miller, R. Blumer, T. Petty, M. Stevens, D. Teale, and M. Smith, "Polarization sensing for target acquisition and mine detection," in *Proceedings SPIE*, vol. 4133, 2000.

[3] Sadjadi F. and C. Chun, "Automatic detection of small objects from their infrared state-of-polarization vectors," *Optics Letters*, vol. **28**, no. 7, pp. 531–533, 2003.

[4] Gurton K., M. Felton, R. Mack, D. LeMaster, C. Farlow, M. Kudenov, and L. Pezzaniti, "MidIR and LWIR polarimetric sensor comparison study," in *Proceedings SPIE 7672*, 2010.

[5] Ratliff B., D. LeMaster, R. Mack, P. Villeneuve, J. Weinheimer, and J. Middendorf, "Detection and tracking of RC model aircraft in LWIR microgrid polarimeter data," in *Proceedings SPIE*, vol. 8160, p. 1, 2011.

[6] Goudail F. and J. S. Tyo, "When is polarimetric imaging preferable to intensity imaging for target detection?," *Journal of the Optical Society of America A*, vol. **28**, pp. 46–53, Jan 2011.

[7] Thilak V., D. Voelz, and C. Creusere, "Image segmentation from multi-look passive polarimetric imagery," in *Proceedings SPIE*, vol. 6682, 2007.

[8] Wolff L., "Polarization-based material classification from specular reflection," *Pattern Analysis and Machine Intelligence, IEEE Transactions on*, vol. **12**, no. 11, pp. 1059–1071, 1990.

[9] Thilak V., D. Voelz, and C. Creusere, "Polarization-based index of refraction and reflection angle estimation for remote sensing applications," *Applied Optics*, vol. **46**, no. 30, pp. 7527–7536, 2007.

[10] Hyde IV M., J. Schmidt, M. Havrilla, and S. Cain, "Determining the complex index of refraction of an unknown object using turbulence-degraded polarimetric imagery," *Optical Engineering*, vol. **49,** no. 12, pp. 126201–126201, 2010.

[11] Koshikawa K., "A polarimetric approach to shape understanding of glossy objects," in *Proceedings of the 6th International Joint Conference on Artificial Intelligence-Volume 1*, pp. 493–495, Morgan Kaufmann Publishers Inc., 1979.

[12] Tyo J., M. Rowe, E. Pugh Jr, N. Engheta, *et al.*, "Target detection in optically scattering media by polarization-difference imaging," *Applied Optics*, vol. **35**, no. 11, pp. 1855–1870, 1996.

[13] Chenault D. and J. Pezzaniti, "Polarization imaging through scattering media," *SPIE Proceedings 4133*, 2000.

[14] Egan W., *Photometry and polarization in remote sensing*. Elsevier, New York, NY, 1985.

[15] Tyo J. S., D. L. Goldstein, D. B. Chenault, and J. A. Shaw, "Review of passive imaging polarimetry for remote sensing applications," *Applied Optics*, vol. **45,** no. 22, pp. 5453–5469, 2006.

[16] Schott J., *Fundamentals of Polarimetric Remote Sensing*. SPIE Press, Bellingham, WA, 2009.
[17] Goldstein D., *Polarized Light, Revised and Expanded*. CRC Press, 2010.
[18] Chipman R., "Polarimetry," in *Handbook of Optics, Third Edition Volume I: Geometrical and Physical Optics, Polarized Light, Components and Instruments (set)*, 3rd edn, ch. 15, New York, NY: McGraw-Hill, 2010.
[19] Goodman J. W., *Statistical Optics*, New York, John Wiley & Sons, Inc., 1985.
[20] Collett E., *Field Guide to Polarization*. SPIE Press, Bellingham, WA, 2005.
[21] Hoffman K. and R. Kunze, *Linear Algebra*. Prentice-Hall, Englewood Cliffs, NJ, 1971.
[22] Priest R. G. and T. A. Gerner, "Polarimetric BRDF in the microfacet model: theory and measurements," tech. rep., DTIC Document, 2000.
[23] Pedrotti F. and L. Pedrotti, *Introduction to Optics*, 2nd edn, Prentice Hall, 1993.
[24] Sandus O., "A review of emission polarization," *Applied Optics*, vol. **4**, no. 12, pp. 1634–1642, 1965.
[25] Resnick A., C. Persons, and G. Lindquist, "Polarized emissivity and Kirchhoff's law," *Applied Optics*, vol. **38**, no. 8, pp. 1384–1387, 1999.
[26] Tyo J. S., B. M. Ratliff, J. K. Boger, W. T. Black, D. L. Bowers, and M. P. Fetrow, "The effects of thermal equilibrium and contrast in lwir polarimetric images," *Opt. Express*, vol. **15**, pp. 15161–15167, Nov 2007.
[27] Eismann M. T., *Hyperspectral Remote Sensing*. SPIE Press, Bellingham, WA, 2012.
[28] Bohren C. F. and D. R. Huffman, *Absorption and Scattering of Light by Small Particles*. Wiley-VCH Verlag GmbH & Co. KGaA, 2008.
[29] Pust N. J., J. A. Shaw, and A. R. Dahlberg, "Concurrent polarimetric measurements of painted metal and illuminating skylight compared with a microfacet model," *SPIE Proceedings 7461*, 2009.
[30] Lin S.-S., K. M. Yemelyanov, J. Edward N. Pugh, and N. Engheta, "Separation and contrast enhancement of overlapping cast shadow components using polarization," *Optics Express*, vol. **14,** pp. 7099–7108, Aug 2006.
[31] Pust N. J. and J. A. Shaw, "Wavelength dependence of the degree of polarization in cloud-free skies: simulations of real environments," *Optics Express*, vol. **20**, pp. 15559–15568, Jul 2012.
[32] Pust N. J., J. A. Shaw, and A. Dahlberg, "Visible-NIR imaging polarimetry of painted metal surfaces viewed under a variably cloudy atmosphere," *Proceedings of the SPIE 6972*, 2008.
[33] Pust N. J., A. R. Dahlberg, M. J. Thomas, and J. A. Shaw, "Comparison of full-sky polarization and radiance observations to radiative transfer simulations which employ AERONET products," *Optics Express*, vol. **19**, pp. 18602–18613, Sep 2011.
[34] Miller M., R. Blumer, and J. Howe, "Active and passive SWIR imaging polarimetry," *Proceedings of the SPIE 4481*, 2002.
[35] Shaw J. A., "Degree of linear polarization in spectral radiances from water-viewing infrared radiometers," *Applied Optics*, vol. **38**, no. 15, pp. 3157–3165, 1999.
[36] Shaw J. A., "Polarimetric measurements of long-wave infrared spectral radiance from water," *Applied Optics*, vol. **40**, no. 33, pp. 5985–5990, 2001.
[37] Felton M., K. P. Gurton, J. L. Pezzaniti, D. B. Chenault, and L. E. Roth, "Measured comparison of the crossover periods for mid- and long-wave IR (MWIR and LWIR) polarimetric and conventional thermal imagery," *Optics Express*, vol. **18**, pp. 15704–15713, Jul 2010.
[38] Tyo J., "Noise equalization in stokes parameter images obtained by use of variable-retardance polarimeters," *Optics Letters*, vol. **25**, no. 16, pp. 1198–1200, 2000.
[39] Tyo J., "Design of optimal polarimeters: maximization of signal-to-noise ratio and minimization of systematic error," *Applied Optics*, vol. **41**, no. 4, pp. 619–630, 2002.
[40] Ambirajan A. and D. Look Jr, "Optimum angles for a polarimeter: part I," *Optical Engineering*, vol. **34**, no. 6, pp. 1651–1655, 1995.
[41] LaCasse C., R. Chipman, and J. Tyo, "Band limited data reconstruction in modulated polarimeters," *Optics Express*, vol. **19**, no. 16, pp. 14976–14989, 2011.

[42] Tyo J. S., C. F. LaCasse, and B. M. Ratliff, "Total elimination of sampling errors in polarization imagery obtained with integrated microgrid polarimeters," *Optics Letters*, vol. **34**, no. 20, pp. 3187–3189, 2009.

[43] Goodman J., *Introduction to Fourier Optics*. McGraw-Hill Companies, 1988.

[44] Ratliff B. M., C. F. LaCasse, and J. S. Tyo, "Interpolation strategies for reducing IFOV artifacts in microgrid polarimeter imagery," *Optics Express*, vol. **17**, pp. 9112–9125, May 2009.

[45] LeMaster D., "Stokes image reconstruction for two-color microgrid polarization imaging systems," *Optics Express*, vol. **19**, no. 15, pp. 14604–14616, 2011.

[46] Ratliff B., C. LaCasse, and J. Tyo, "Adaptive strategy for demosaicing microgrid polarimeter imagery," in *Aerospace Conference, 2011 IEEE*, pp. 1–9, IEEE, 2011.

[47] Hardie R., D. LeMaster, and B. Ratliff, "Super-resolution for imagery from integrated microgrid polarimeters," *Optics Express*, vol. **19**, no. 14, pp. 12937–12960, 2011.

[48] LaCasse C., J. Tyo, and R. Chipman, "Role of the null space of the DRM in the performance of modulated polarimeters," *Optics Letters*, vol. **37**, no. 6, pp. 1097–1099, 2012.

[49] Black W. T., C. F. LaCasse IV, and J. S. Tyo, "Frequency-domain scene-based non-uniformity correction and application to microgrid polarimeters," in *Proceedings SPIE 8160*, 2011.

[50] Ratliff B. M. and D. A. LeMaster, "Adaptive scene-based correction algorithm for removal of residual fixed pattern noise in microgrid image data," in *Proceedings SPIE 8364*, 2012.

[51] Persons C., M. Jones, C. Farlow, L. Morell, M. Gulley, and K. Spradley, "A proposed standard method for polarimetric calibration and calibration verification," in *Proceedings of the SPIE*, vol. 6682, 2007.

[52] Scharf L., *Statistical Signal Processing: Detection, Estimation, and Time Series Analysis*. Addison – Wesley, Reading, MA, 1991.

[53] Reed I. S. and X. Yu, "Adaptive multiple-band CFAR detection of an optical pattern with unknown spectral distribution," *Acoustics, Speech and Signal Processing, IEEE Transactions on*, vol. **38**, no. 10, pp. 1760–1770, 1990.